



Genesis and evolution of the San Manuel iron skarn deposit (Betic Cordillera, SW Spain)

Igor González-Pérez^{a,*}, José M. González-Jiménez^{a,b}, Fernando Gervilla^{a,b}, Isabel Fanlo^c, Fernando Tornos^d, Vanessa Colás^e, Enrique Arranz^c, John Hanchar^f, María del Mar Abad-Ortega^g, Antonio J. Moreno-Abril^a, María Carrión^h, Samuel Noval^c

^a Departamento de Mineralogía y Petrología, Facultad de Ciencias, Universidad de Granada, Avda. Fuentenueva s/n, 18002 Granada, Spain

^b Instituto Andaluz de Ciencias de la Tierra (IACT), CSIC-UGR, Avda. de las Palmeras 4, 18100 Armilla, Granada, Spain

^c Departamento de Ciencias de la Tierra, Cristalografía y Mineralogía, Universidad de Zaragoza, Pedro Cerbuna 12, 50009 Zaragoza, Spain

^d Instituto de Geociencias (IGEO, CSIC-UCM), c/Severo Ochoa, 7, 28040 Madrid, Spain

^e Instituto de Geología, Universidad Nacional Autónoma de México, Ciudad Universitaria, 04510 Ciudad de México, Mexico

^f Memorial University of Newfoundland, St. John's NL A1B 3X5, Canada

^g Centro de Instrumentación Científica (CIC-UGR), Paseo del Prof. Juan Ossorio, s/n. Campus Universitario de Fuentenueva, 18071 Granada, Spain

^h Facultat de Ciències, Universitat Autònoma de Barcelona, 08193 Bellaterra, Spain

ARTICLE INFO

Keywords:

Magnesioferrite
Magnetite
Mg-skarn
Ronda peridotites
Spinel exsolution
LA-ICP-MS

ABSTRACT

The San Manuel magnesian skarn is an iron deposit hosted in dolomitic marbles from a tectonic slice imbricated within the Ronda peridotites, in the westernmost part of the Betic Cordillera, Spain. According to the dominant mineral assemblage, the skarn is subdivided into three different zones, (1) forsterite ± calcite skarn, (2) calcite ± chlorite ± serpentine skarn, and (3) Ca-amphibole skarn. The main ore in the skarn is a ~ 2.5 m thick, massive ore body situated in the middle of the sequence. In this paper, we firstly report a comprehensive major to trace element composition, texture, microstructure, and mineralogy characterization for zoned magnesioferrite-magnetite grains of the San Manuel deposit using a combination of (1) laser ablation inductively coupled plasma mass spectrometer, (2) focused ion beam combined with transmission electron microscopy, and (3) electron back-scattered diffraction. We have defined four different magnesioferrite-magnetite generations. A complete sequence of zoning includes cores of magnesioferrite (Mag-1; MgO up to 10.6 wt%) overprinted by three successive generations of magnetite, namely Mag-2, Mag-3, Mag-4. Mag-2 (MgO < 4 wt%), hosts composite forsterite ± calcite ± chlorite inclusions, consistently with high Si, Ca, and Sr (average: 8204 ppm, 8980 ppm, and 49 ppm respectively) contents detected by in situ laser ablation inductively coupled plasma (LA-ICP-MS). Mag-3 replacing former Mag-1 and Mag-2 includes nanometric spinel and gahnite exsolutions detected by focused ion beam combined with a transmission electron microscope (FIB-TEM), which is consistent with its high Al, Ti, V, and Ga (average: 5073 ppm, 368 ppm, and 20 ppm, respectively) trace element concentration. Mag-4 is the Fe-richest magnetite (up to 94.16 wt% FeO_{total}) forming the outermost rims in magnetite grains, and exhibiting the lowest total trace element contents. Approaches in temperature estimations employing magnetite-spinel exsolutions in Mag-3 suggest that the minimum temperature of the prograde stage reached temperatures below 700 °C, whereas Mag-4 should be formed during the retrograde stage. Magnetite microstructure studied by electron backscatter diffraction (EBSD) suggests Mag-4 formation under fluid-assisted dynamic conditions, which is consistent with the tectonic evolution of the emplacement. We propose that the San Manuel deposit formed by pulsed hydrothermal fluids derived from anatexis of crustal rocks during peridotite emplacement, promoting re-equilibration processes that led to the magnesioferrite-magnetite zoning.

* Corresponding author.

E-mail address: igorgonzpe@ugr.es (I. González-Pérez).

<https://doi.org/10.1016/j.oregeorev.2021.104657>

Received 6 September 2021; Received in revised form 16 December 2021; Accepted 17 December 2021

Available online 22 December 2021

0169-1368/© 2021 The Author(s). Published by Elsevier B.V. This is an open access article under the CC BY license (<http://creativecommons.org/licenses/by/4.0/>).

1. Introduction

Skarn deposits are one of the most abundant ore types in the Earth's crust widely distributed around the world (Zharikov 1970; Einaudi et al. 1981; Meinert et al. 2005; Fei et al. 2019). This type of deposits that have formed in rocks of almost all ages contain ores contributing to important resources of several base (Fe, Cu, Pb, Zn, W, Mo, Sn; e.g., Zhang et al., 2013; Zhang et al. 2014; Jansson and Allen, 2015; Xie et al. 2015; Zhao et al. 2017; Yu 2019; Kuşçu 2019; Chen et al. 2020; Xie et al. 2021) and precious metals (Au, Ag; e.g., Cepedal et al. 2000; Logan 2000; Pons et al. 2010; Mao et al. 2017; Xie et al. 2019, Guo et al. 2020) as well as other elements of industrial interest (REE, U, B; e.g., Aleksandrov and Troneva 2008; Bilohušćin et al. 2017; Marincea and Dumitras, 2019). Skarn deposits are formed by metamorphic and metasomatic processes, commonly by the interaction of carbonate rocks and silicate fluids. It may include fluids of magmatic, metamorphic, meteoric, and/or marine origin (Meinert et al. 2005).

Most major skarn deposits are directly related to igneous activity. Broad correlations between igneous composition and skarn type have been described by several workers (Meinert, 1992 and references therein). For example, Sn and Mo skarns are typically associated with high silica, strongly differentiated plutons whereas magnesian iron skarns are associated with diverse plutons in a variety of tectonic settings; the unifying feature is that they all form from dolomitic wall rock (Einaudi and Burt 1982; Zharikov 1970; Zharikov et al. 2007). Magnesian skarns (Mg-skarn) are of particular interest as they typically contain the largest resources of iron ores (Einaudi et al. 1981; Zhang et al. 2021 and references therein; Pampa del Pongo, Peru, Calvo et al. 2013; the biggest Mg-skarn deposit). Many researchers have investigated the origin and evolution of magnesian iron skarns deposits using magnetite trace element geochemistry as a fingerprint (e.g., Huang et al. 2016; Hu et al. 2017; Mirzaei et al., 2018; Chen et al. 2020; Sarjoughian et al. 2020). However, the trace element composition of hydrothermal magnetite in such types of deposits is strongly influenced by several factors including (1) composition of the melt/fluid; (2) rates of melt-fluid/rock interaction; (3) element partitioning amongst magnetite and co-precipitating minerals, (4) physicochemical conditions of the melt/fluid (e.g., pressure, temperature, fO_2) and (5) nano-to-micro sized inclusions in magnetite (Carew 2004; Dupuis and Beaudoin 2011; Dare et al. 2014; Nadoll et al. 2012, Nadoll et al., 2014; Hu et al. 2014, Hu et al., 2015, Hu et al., 2017; Sun et al. 2017; Mei et al. 2017; Wang et al. 2018). Noteworthy, the abundance of a single trace element may also be influenced by more than one factor, which limits the use of geochemistry in magnetite alone as a tool to fingerprint the origin of the iron ores (e.g., Velasco et al. 2016, Broughm et al. 2017). A more reliable way to distinguish different magnetite generations, and therefore the genesis and evolution of the skarn deposits is the combination of magnetite geochemistry with a careful micro- and nano-scale textural and mineralogical study (e.g., Hu et al. 2014; Deditius et al. 2018).

In this paper, we report the first-ever careful study of the mineralogy and magnetite geochemistry from the San Manuel iron skarn deposit in SW Spain. The singularity of this deposit is that it is hosted in dolomitic marbles of the contact aureole produced by the crustal emplacement of the Ronda peridotites (southern Spain) — the largest outcrops of Subcontinental Lithospheric Mantle peridotites exposed on the Earth's surface (Gervilla et al. 2019 and references therein). This is a very uncommon geological framework for the formation of an iron skarn deposit, which offers a unique opportunity to better constrain the physicochemical conditions of this type of mineral deposit worldwide. Of particular interest is to evaluate the balance between the nature of the infiltrating fluids and host rock for the formation of this unusual iron skarn deposit. To achieve these goals, we present and discuss novel micro-analytical data obtained using in-situ laser ablation techniques for a suite of key minerals and elements of the mineralization, i.e., (1) major-, minor- and trace-element compositions of oxides by electron probe micro-analyzer (EPMA) and laser ablation inductively coupled

plasma mass spectrometry (LA-ICP-MS), and (2) focused ion beam transmission electron microscopy (FIB-TEM). We also evaluate the effects that deformation may have on the chemistry of composite magnesioferrite-magnetite crystals using Electron Back-scattered Diffraction (EBSD). These data are integrated into an innovative model that links the genesis of the iron skarn deposit to fluids released during dehydration of metasediments during the hot emplacement of the mantle peridotites into the continental crust. Multiple pulses of hydrothermal fluids led to replacement and re-equilibration processes and subsequent different magnesioferrite-magnetite generations in terms of microstructure, chemistry, and mineralogy of solid inclusions.

2. Geological setting

2.1. Regional geology

The San Manuel Mg-skarn is situated in Sierra Bermeja, approximately 5 km northwards of the city of Estepona, southern Spain (Fig. 1). Geologically it belongs to the Alpujarride Complex, one of the three tectonic nappes that constitute the Internal Zone of the Betic orogenic belt: the Nevado Filábride Complex at the bottom, the Alpujarride Complex in the middle, and the Maláguide Complex at the top of the tectonic sequence (Egeler and Simons 1969).

The Betic-Rif orogenic belt is located in the westernmost part of the Mediterranean region and comprises the Betic Cordillera in southern Spain, and the Rif in north Morocco (Fig. 1a). This orogenic Belt was assembled from Late Cretaceous to Tertiary as a result of the convergence between Iberia and Africa and the collision of the Alborán domain with the south Iberian and Maghrebian passive margins (Andrieux et al. 1971; Durand-Delga and Fontboté 1980; Dewey et al. 1989; Balanyá and García-Dueñas 1987). The Geology of the Betic Cordillera is subdivided into three main geological domains: External Zones, Internal Zones, and the Flysch, the latter sandwiched between the other two domains. The External Zones are located to the north of the Betic Cordillera and correspond to the sedimentary cover deposited during the Mesozoic to Cenozoic on the Iberian foreland. As noted above, the Internal Zones consist of three nappe complexes (Nevado Filábride, Alpujarride, and Maláguide), which correspond to sediments deposited between Iberia and Africa plates during Paleozoic to Mesozoic times, tectonically stacked against the Iberian margin and subsequently metamorphosed at different grades during the Alpine orogeny. The Flysch is composed of turbiditic sediments deposited from Cretaceous to Miocene in deep marine basins located in the current Alborán sea (Vissers et al. 1995).

For the sake of clarity, the Alpujarride Complex in the studied area comprises two main units, which from bottom to top are: the Blanca unit (formed by the Ojén, Guadaiza and Yunquera nappes) and the Los Reales unit (Navarro-Vilá and Tubía 1983; Tubía and Cuevas 1986; Tubía et al. 2013). The lowest part of the Los Reales nappe hosts the so-called peridotites of the Serranía de Ronda, which constitutes the main relief of the Sierra Bermeja located north of the city of Estepona (Fig. 1b). Here, peridotites crop out in three separate massifs: Ronda, thought as the largest (~300 km²) exposure of subcontinental lithospheric mantle (SCLM) peridotite on Earth surface, Ojén (~70 km²), and Carratraca (~60 km²) (Fig. 1b). These massifs mostly consist of lherzolites and harzburgites with minor amounts of dunite as well as different types of pyroxenite layers, locally intruded by leucocratic dykes (Obata 1980; Van der Wal and Vissers 1993, 1996; Garrido and Bodinier 1999; Acosta-Vigil et al. 2014). These peridotites are exposures of a Proterozoic (1.2–1.8 Ga) SCLM (Reisberg and Lorand 1995; Marchesi et al. 2010; González-Jiménez et al. 2013a, González-Jiménez et al., 2013b) finally emplaced in the crust during Late Oligocene/Early Miocene (e.g., Esteban et al. 2004; Esteban et al., 2007; Esteban et al., 2010; Precigout et al., 2007; González-Jiménez et al. 2017). The exhumation and final emplacement of peridotites into the continental crust was related to the episode of extension of the Betic-Rif orogenic belt that gave rise to the formation of the Alborán marine basin, probably during the

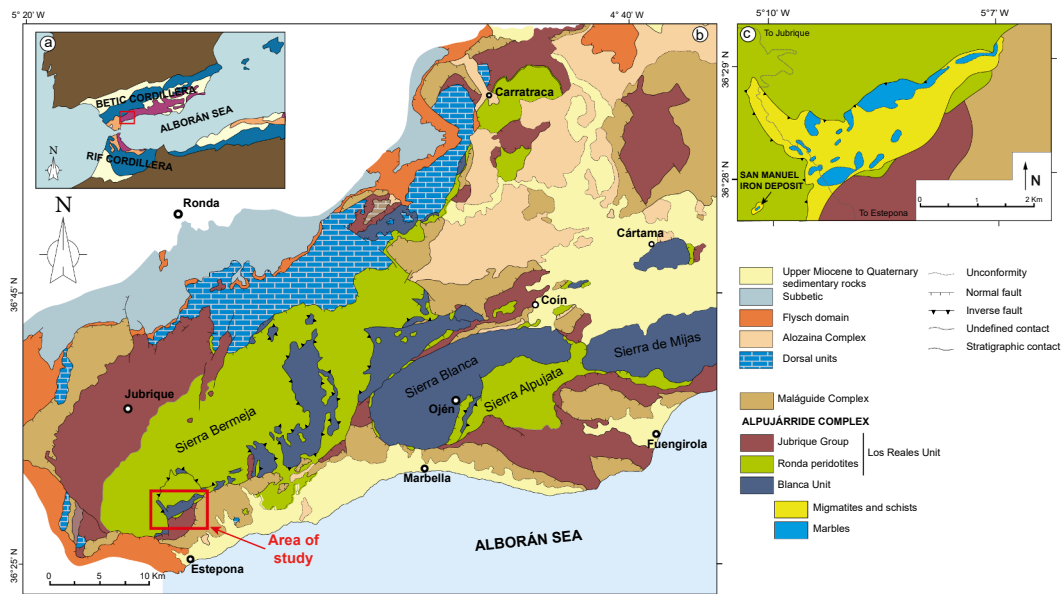


Fig. 1. (a) Localization of the Betic Cordillera within the western Mediterranean Basin; keys: Pale-yellow: Neogene sediments; Blue: South-Iberian and Magrebian domains; Purple: Alborán domain; Orange: flysch domain. (b) Geological map of southern Spain modified from Gervilla et al. (2019) showing the three main peridotite massifs cropping out in the Betic Cordillera: Ronda (~300 km²), Ojén (~70 km²), and Carratraca (~60 km²), from Gervilla et al. (2019). The red rectangle marks the localization of the San Manuel Skarn. (c) Local geological map showing the localization of the San Manuel skarn.

development of a back-arc basin behind the Betic-Rif orogenic wedge (Garrido et al. 2011; Marchesi et al. 2012; Hidas et al. 2013, Hidas et al., 2015). Within the Los Reales nappe, the peridotites are overlain by a thick (up to 7 km) sequence of metapelitic rocks that show a decreasing metamorphic grade upwards from the contact with the peridotites (i.e., from acidic granulites (kinzigites), gneisses and migmatites, to schist, phyllites and, locally, marbles; Balanyá et al., 2007; Tubía et al. 1997; Platt et al. 2013); these rocks correspond to vestiges of a pre-Mesozoic continental crust that also experienced substantial thinning during Late Oligocene/Early Miocene. In contrast, peridotites of the Los Reales unit thrust over a typical Alpujarride sequence of the Blanca unit composed of upper carbonate-rich metasedimentary unit (i.e., Triassic dolomitic marbles) that contains relative abundant bodies of amphibolite (Tubía et al. 1997; Sánchez-Rodríguez and Gebauer 2000), lying on high-grade metapelites and migmatites containing zircons with crystallization ages of ~ 280–290 Ma and a later thermal and fluid overprint ca. 30 Ma (Acosta-Vigil et al. 2014).

Leucocratic dykes with a wide range of compositions (i.e., granite, granodiorite, monzonite, and transitional rocks between these end-members) intrude the crustal rocks of the Blanca units as well as the ultramafic rock themselves. These intrusions dated between 22 and 18 Ma corresponding to small fractions of acidic melts originated by partial melting of the underlying migmatites during the hot emplacement of the peridotites into the continental crust in Late Oligocene/Early Miocene (Sánchez-Rodríguez and Gebauer 2000; Pereira et al. 2003; Cuevas et al. 2006; Esteban et al. 2007, Esteban et al., 2010; González-Jiménez et al. 2017).

From a metallogenic point of view, the ultramafic massifs of the Serranía de Ronda are characterized by the occurrence of different types of ore deposits found inside and along with the contact of the ultramafic bodies with upper crustal rocks. The assemblage of ores hosted in the ultramafic rocks comprises Cr, Ni, Cu, and PGE magmatic ores distributed according to the petrological-structural domains of the ultramafic massifs (see Gervilla et al. 2019 and references therein). This assemblage that is unique in the world includes (Gervilla and Leblanc 1990): (1) sulfide-graphite (S-G) ores, (2) chromium (Cr) ores, and (3) chromium-nickel (Cr-Ni) ores. In contrast, the orebodies found at the contact between the ultramafic rocks and the dolomitic marbles of the Blanca unit include several known skarn-related deposits: El Peñoncillo (also known

as La Concepción), La Vibora, El Cañuelo (also known as El Robledal), Conchita Mine, Lucía Mine, and San Manuel (Gervilla et al. 2019 and references therein); the latter is the subject of the current study.

2.2. Geology of the San Manuel deposit

The San Manuel deposit is located in the Sierra Bermeja, southern Spain, in a Fe-rich metallogenic area including W, Bi, and Sn mineralizations (e.g., El Robledal, La Vibora, El Peñoncillo) also located at the contact between the mantle peridotites of the Serranía de Ronda and crustal units. It has been intermittently mined for iron from the middle of the 19th century till the late 20th century, with an estimation of exploited resources of 51750 tons Fe @ 68% (Gervilla et al. 2019 and references therein). The main mineralization at the skarn consists of a single massive orebody up to 2.5 m thick and 30 m long, conformably oriented to the dolomitic marble (ore zone in Fig. 3a-g), which roughly separates upper Fo-Cal skarn from lower Cal-Chl-Srp skarn. This orebody displays all magnesioferrite-magnetite generations (i.e., from Mag-1 to Mag-4), ranging in size from < 20 μm up to > 100 μm and forming 120° triple junctions (Fig. 8a). The massive body grades outwards to semi-massive and disseminated ore (Fig. 8b-d), where ore minerals are interstitial to forsterite (Fig. 8b) and/or embedded within the host carbonates (Cal-1; Fig. 8c-d). Several small pods and lenses of massive ores grading outwards to vein-like mineralization are also recognized (Fig. 5a). Disseminated ores are also common in the whole skarn sequence, with sizes ranging from 10 μm to 500 μm. Mag-1 and Mag-2 are widespread in the Fo-Cal skarn whereas Mag-3 dominates in the Cal-Chl-Srp skarn. Outer rims of Mag-4 that commonly form the 120° triple junction occur in the whole sequence.

The deposit is hosted in a package of dolomitic marbles of the Blanca unit (~25 m thick) overlying migmatites (~15 m thick), both forming a tectonic slice imbricated within the lower thrust of the southern contact of the Ronda peridotite (Figs. 1c and 2). The migmatite exhibit nebulitic to diatexitic microstructure and contain abundant relicts of metapelites. They are interpreted as the product of the partial melting of former metapelitic rocks of the Blanca unit during the hot thrusting of the mantle peridotites over these crustal rocks (Torres-Roldán 1983; Tubía et al. 1997, Tubía et al., 2013; Esteban et al. 2008). Acosta-Vigil et al. (2014) identified zircons of variscan age of ca. 280–290 Ma in these

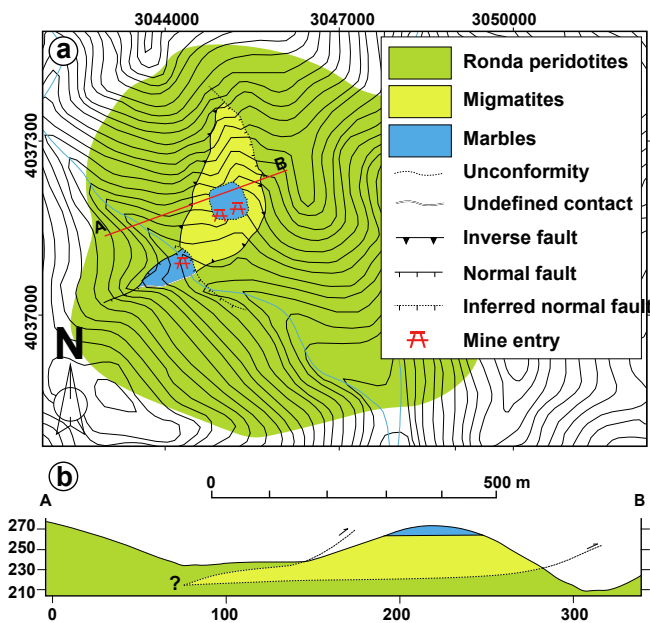


Fig. 2. (a) Geological map of the San Manuel skarn deposit including localization of A-B cross-section. (b) Schematic cross-section of the San Manuel skarn. Note the imbrication of the tectonic slide within the Ronda peridotites.

migmatites, recording a late thermal overprint during the Miocene (ca. 30 Ma). In contrast, U-Pb SHRIMP dating of zircons on migmatites equivalent to those found at San Manuel in the Guadaiza nappe cropping out at the north of Sierra Bermeja yielded a crystallization age of 22.3 ± 0.7 Ma (Esteban et al. 2010). The latter age accounts for a Miocene emplacement of peridotites and subsequent partial melting of metapelites, according to previous geochronological data indicating the intrusion of anatectic granitic dikes ca. 23–17 Ma (Sanchez-Rodríguez, 1998; Cuevas et al. 2006; González-Jiménez et al. 2017).

2.2.1. Skarn zones

Zoning of the skarn is distinguishable in the field, revealing that 20 m of the total 25 m exposed are affected by the alteration, which resulted, from top to bottom, in the following three main skarn zones (Fig. 3a):

Forsterite-calcite skarn (Fo-Cal skarn). This zone comprises the upper 9 m of the exposed section (Fig. 3a-c), consisting of host dolomitic marble and skarn minerals. The uppermost part of the sequence (~4 m) consists of an interlocking mosaic of millimeter-sized dolomite crystals (Fig. 4a). Downwards, they preserve the interlocking mosaic texture along with euhedral magnetite disseminations, where dolomite crystals are smaller (Fig. 4b). Locally, dolomite is partially replaced with calcite. Minor granular, millimeter-sized forsterite crystals are also found dispersed within the dolomite matrix. In the lowermost part of the Fo-Cal skarn (~2 m), forsterite forms nearly monomineralic domains, which can be partially replaced by brownish calcite. In the lowest zones of the Fo-Cal skarn, forsterite is also replaced by chlorite \pm chrysotile (Fig. 4c-f).

Calcite-chlorite-serpentine skarn (Cal-Chl-Srp skarn). This zone corresponds to the lowest ~12 m of the profile (Fig. 3a and d-e), consisting of a hydrous mineral assemblage replacing former anhydrous silicates and carbonates. Thus, dolomite and forsterite are replaced by calcite and chlorite \pm serpentine (antigorite and chrysotile), respectively (Fig. 5a-d). Chlorite also seems to replace calcite (Cal-1) (Fig. 5c-d). There are two different generations of chrysotile. Colorless chrysotile (Ctl-1) is usually associated with antigorite and chlorite as well as related to magnetite boundaries (Figs. 4e-f and 5a-b). Late brown-colored chrysotile (Ctl-2) occurs as late small veins crosscutting the whole skarn sequence (Fig. 5e-f).

Ca-amphibole skarn (Ca-skarn). This is a zone barren of

mineralization embedded in the Cal-Chl-Srp skarn (Fig. 3a and h). It is composed of white-greenish colored amphibole (i.e., pargasite) with minor chlorite, crosscut by calcite veins (Cal-2) (Fig. 6a-b). Monomineralic forsterite domains are also common in the zones adjacent to the Ca-skarn (Fig. 6c). The limit between the Ca-rich skarn and the Cal-Chl-Srp skarn is marked by yellow-colored olivine and carbonate-bearing boundary (Fig. 6d).

2.2.2. Paragenetic relationships

Based on the field and the textural relationship between the ore and gangue minerals we suggest four paragenetic stages of mineralization at San Manuel (Fig. 7):

- (I) **Prograde stage.** During this stage, hydrothermal fluids reacted with host dolomite marble to form forsterite and magnesioferrite (Mag-1), leaching Mg from dolomite. The prograde stage represents the main ore-forming period, as attested by the presence of large amounts of euhedral to anhedral zoned crystals of Mag-1 and Mg-rich magnetite (i.e. Mag-2, Mag-3) coexisting with forsterite. Magnesioferrite grains may be found either interstitially to, as inclusions in, or replacing, forsterite (Figs. 4c-f and 8a-b).
- (II) **Retrograde stage.** In this stage dolomite and minerals formed in the prograde stage were altered and/or crosscut by hydrous and/or carbonate minerals assemblages to varying degrees (Fig. 5). Early-formed forsterite was partially to totally replaced by Cal-1, serpentine, and chlorite (Fig. 4d-f). Antigorite usually occurs as pseudomorphic rims around pre-existing forsterite as well as forming a mesh texture, while Ctl-1 tends to replace former antigorite or be around Fe-oxides (Figs. 4e-f and 5a-b). Ctl-2 forms late veins crosscutting the entire skarn body, especially in those parts where the retrograde stage alteration was intense (Fig. 5e-f). During this stage, a different generation of Mg-poor and Fe-rich magnetite (Mag-4) replaced early-formed Mag-1, Mag-2, and Mag-3.
- (III) **Sulfide stage.** Sulfides are mainly pyrite and to a lesser extent, chalcopyrite (Fig. 3d), which partially replaces all magnesioferrite-magnetite generations through grain boundaries, interstices, or late crack-seal.
- (IV) **Late carbonate stage.** During this stage, Ca-amphiboles domains developed probably at expense of relic forsterite-rich domains embedded in the Cal-Chl-Srp skarn. Veins of late clean calcite-bearing (Cal-2) crosscutting the whole skarn intersect former serpentine (Ctl-2) veins and sulfides as well as the Ca-skarn, attesting their latest origin (Figs. 5e-f and 6a-b).

3. Samples and analytical methods

A list of studied samples is included in Table 1. Analytical procedures are described in detail in electronic Digital Appendix A, and the results are presented in Digital Appendix B to I.

4. Results

4.1. Chemistry of the skarn minerals

The minerals in the skarn can be grouped into three classes: carbonates, anhydrous silicates, and hydrous minerals.

4.1.1. Carbonates

Carbonates include dolomite, Cal-1 replacing dolomite and forsterite, and clean vein-filling calcite (Cal-2) crosscutting the whole skarn sequence. Dolomite, Cal-1, and Cal-2 from the different skarn zones do not show appreciable differences in their chemistry, except for a slightly Ca-enrichment and Fe-depletion in smaller dolomite crystals from the Fo-Cal skarn (Fig. 9a); Appendix B). Thus, dolomite in Fo-Cal skarn exhibits CaO and FeO_{tot} varying from 32.91 to 29.68 wt% and from 0.46

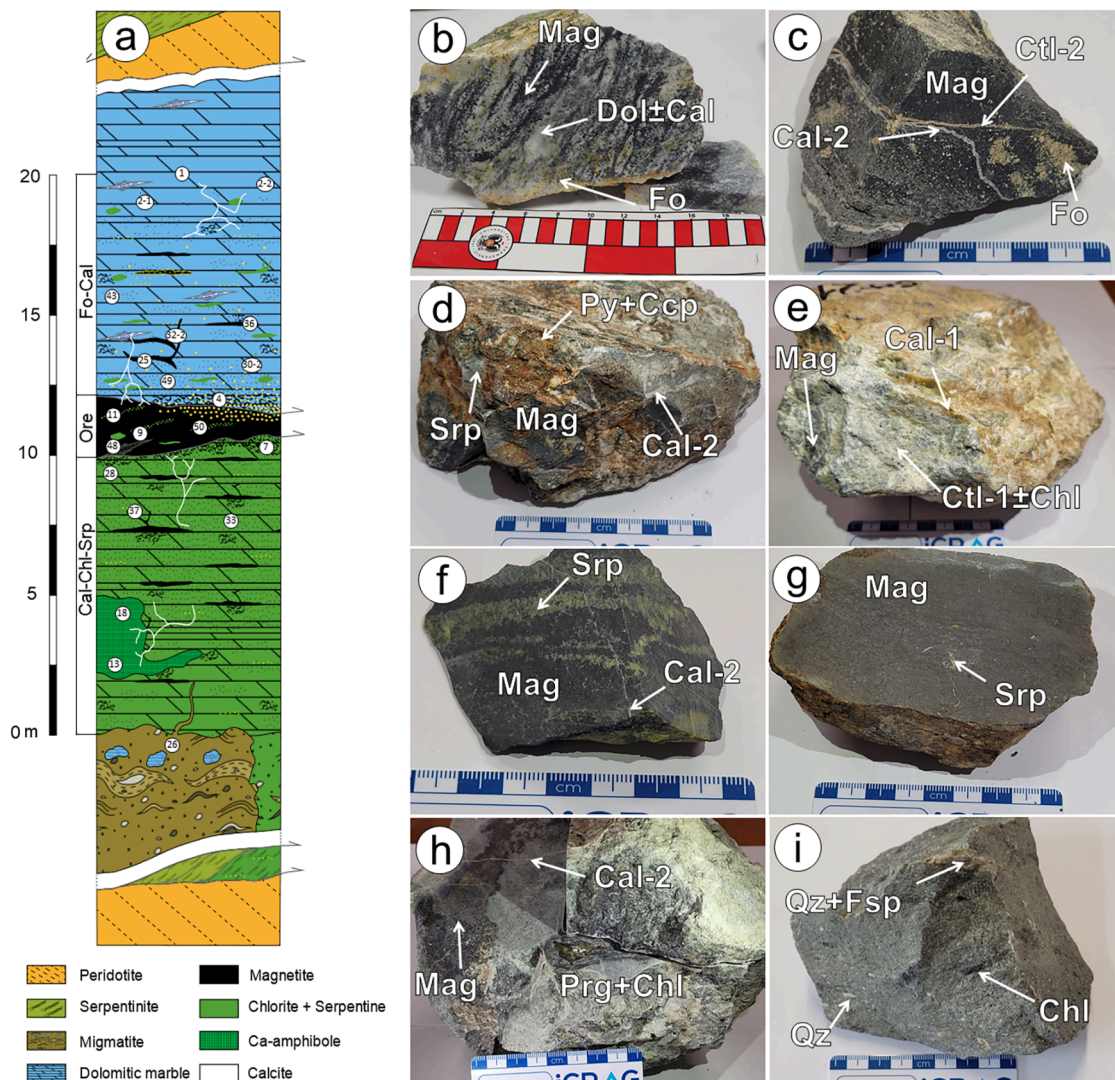


Fig. 3. (a) Schematic stratigraphic column of the San Manuel deposit including the three zones defined within the deposit (i.e., Fo-Cal skarn, Ore, Cal-Chl-Srp). Ca-skarn zone is marked with squared-patterned dark green. Photographs of hand-scale specimen representative from each one of the zones identified in the San Manuel skarn deposit are shown for the sake of clarity in (b) to (i). Mag: magnetite; Dol: dolomite; Cal: calcite; Fo: forsterite; Cal-2: calcite-2; Ctl-2: chrysotile-2; Srp: serpentine; Py: pyrite; Ccp: chalcopyrite; Chl: chlorite; Prg: pargasite; Qz: quartz; Fsp: feldspar. Abbreviations from Whitney and Evans (2010).

to 0.05 wt%, respectively, whereas in the Cal-Chl-Srp skarn CaO and FeO_{tot} range from 29.06 to 28.32 wt% and from 2.10 to 1.66 wt%, respectively. Cal-1 and Cal-2 exhibit similar compositions in all skarn zones, with $\text{MgO} < 1$ wt% and $\text{FeO}_{\text{tot}} < 0.72$ wt%.

4.1.2. Anhydrous silicates

EPMA analyses ($n = 19$) show that there are no compositional variations between forsterite from different skarn zones. However, its composition fluctuates depending upon the presence or not of ore minerals. Where mineralization is massive (i.e., SM-4; Table 1), forsterite is Mg-rich ($\text{MgO} > 57$ wt%), and Fe-poor ($\text{FeO}_{\text{tot}} < 1\%$ wt%), with end-members percentage of $\text{Fo}_{99}\text{-Fa}_1$ (Appendix C). Conversely, in zones with disseminated ores (i.e., SM-49; Fig. 3a; Table 1) as well as in domains located near the contact with the Ca-skarn zone (i.e., SM-18; SM-13; Fig. 3a; Table 1), forsterite contains higher Fe ($\text{FeO}_{\text{tot}} 19.38\text{--}7.32$ wt%) and lower Mg ($\text{MgO} = 51.55\text{--}40.95$ wt%), with an end-members percentage of $\text{Fo}_{93\text{--}79}\text{-Fa}_{7\text{--}21}$. (Fig. 9b). MnO content of forsterite is systematically lower than 0.54 wt%.

4.1.3. Hydrous minerals

This mineral assemblage includes those formed during retrograde

alteration of former skarn minerals.

- (1) *Serpentine*: Two types of serpentine polymorphs have been identified (i.e., antigorite and chrysotile) by mean of single-spot micro-RAMAN analyses (Appendix D), as well as two different generations of chrysotile (i.e., Ctl-1 and Ctl-2). The small size of antigorite and its partially-to-totally replacement to chrysotile did not allow to carry out reliable EPMA analysis. Ctl-1 replacing former antigorite or related to magnetite boundaries (Figs. 4e-f and 5a-b), exhibit $\text{Mg}\# = \text{Mg}/(\text{Mg} + \text{Fe}^{2+}) = 0.98\text{--}0.93$, whereas Ctl-2 shows slightly lower $\text{Mg}\# = 0.95\text{--}0.93$ (Appendix C).
- (2) *Chlorite*: Chlorite occurs forming aggregates with serpentine, partially replacing forsterite and/or carbonates (Fig. 5b-d). They are Mg-rich chlorites ($\text{MgO} = 42.02\text{--}26.13$ wt%) (Table 2; Appendix C) ranging between subspecies of clinochlore and talchlorite according to the classification of Hey (1954) (Fig. 9c; Appendix C). However, there is no marked compositional variation in chlorite from the different skarn zones.
- (3) *Amphibole*: Amphiboles are restricted to zones of the Cal-Chl-Srp skarn sequence in which Ca-skarn overprinted former Mg-skarn. They are green to brown crystals up to 2 mm in size, forming

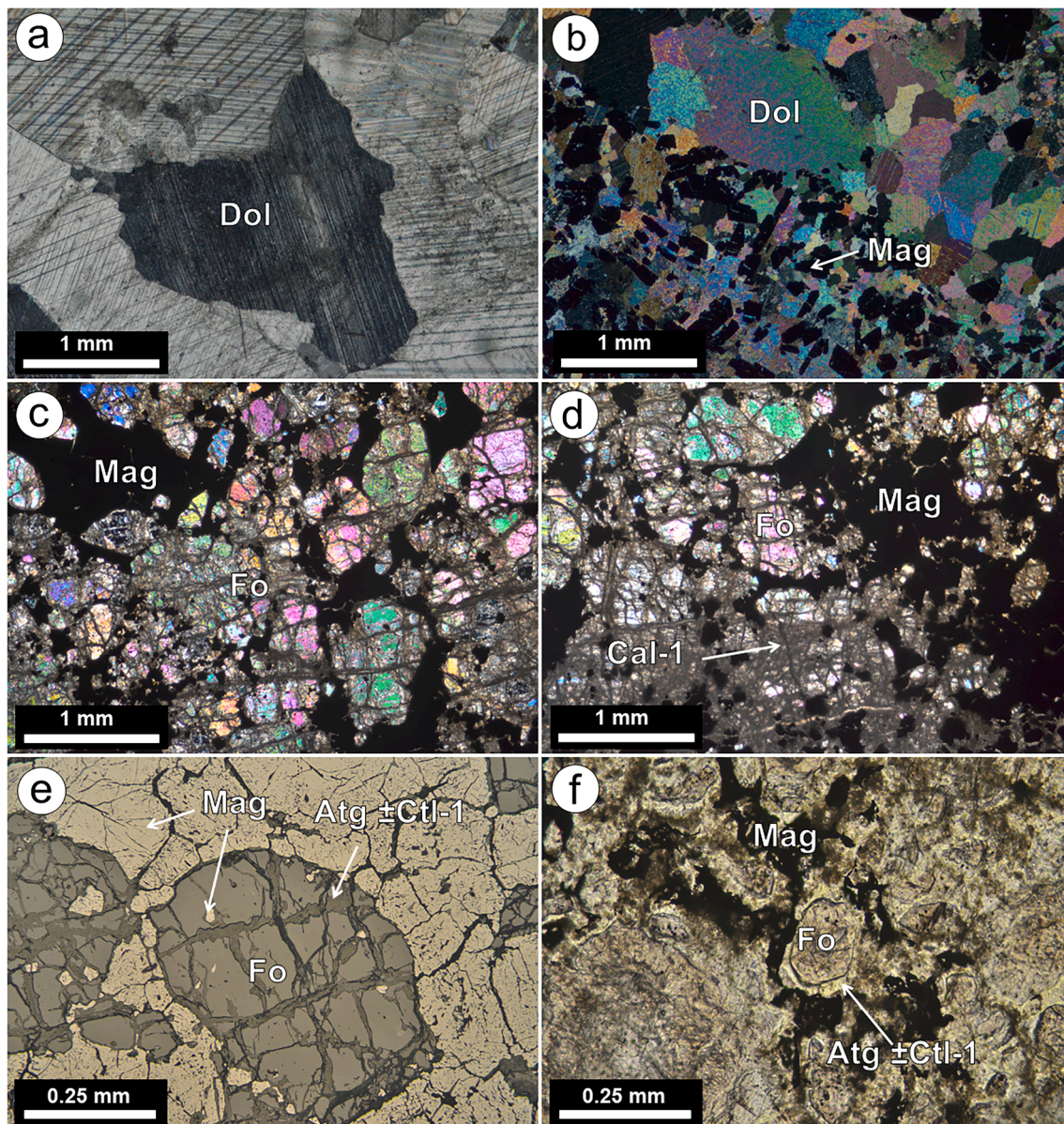


Fig. 4. Photomicrographs of the Fo-Cal skarn from the San Manuel deposit. (a) Dolomite marble from the non-mineralized skarn with typical interlocking texture. (b) Dolomite marble with disseminated magnetite mineralization from the upper Fo-Cal skarn. Note the grain-size reduction of dolomite crystals where magnetite is present. (c) and (d) crossed-polarized light photomicrographs, respectively, of disseminated magnetite mineralization in the Fo-Cal skarn. The increase of calcite amount replacing forsterite downwards is shown in (d). (e) Reflected light photomicrograph of intergranular and forsterite-included magnetite. Mesh-textured forsterite is crosscut by serpentine minerals. (f) Forsterite is replaced by serpentine minerals. This photomicrograph shows partially replaced forsterite from the Fo-Cal skarn. Dol: dolomite; Mag: magnetite; Fo: forsterite; Cal-1: calcite-1; Atg: antigorite; Ctl-1: chrysotile-1. Abbreviations from [Whitney and Evans \(2010\)](#).

almost monomineralic aggregates, with minor intergranular chlorite ([Fig. 6a-b](#)). All the analyzed grains ($n = 4$) are calcic amphiboles overlapping the compositional field of pargasite ([Fig. 9d](#); Appendix C).

4.2. Mineralogy of iron oxides

4.2.1. Zoning of iron oxides

The striking feature of the skarn is the presence of variably zoned magnesioferrite-magnetite, which have been grouped in three different zonings based on textural and mineral assemblage relationships, chemical variations, as well as the different mineralogy of their inclusions. (1) A complete sequence of zoning includes cores of Mag-1 overprinted by three successive generations of magnetite, namely Mag-2, Mag-3, Mag-4 ([Fig. 10](#)); this type of zoning was found in a semi-

massive sample collected in the proximities of the main orebody (SM-48; [Fig. 3a](#); [Table 1](#)). (2) Cores of Mag-1 partly or fully replaced by Mag-2, and Mag-4 rims dominate in the Fo-Cal skarn ([Fig. 11a-c](#)), whereas lacks in Cal-Chl-Srp skarn. (3) Cores of Mag-3 rimmed by Mag-4 are the commonest zoning in the Cal-Chl-Srp skarn ([Fig. 11d-i](#)), while almost absent in the Fo-Cal zone. They typically show a narrow Mag-4 rim compared to wide spinel-rich cores of Mag-3. This zoning is well-defined in grains forming massive to semi-massive ore, where they exhibit polygonal textures defining 120° triple junctions ([Fig. 11d, g](#)).

4.2.2. Iron oxide chemistry

[Fig. 12](#) shows the analyzed grains composition plotted in a $Fe^{2+\#} = Fe/(Fe^{2+}+Mg)$ vs. $Fe^{3+\#} = Fe^{3+}/(Fe^{3+}+Al^{3+})$ diagram. Mag-1 falls within the boundary of magnesioferrite-magnetite fields, according to the highest MgO (7.56–10.67 wt%) and relatively high FeO_{tot}

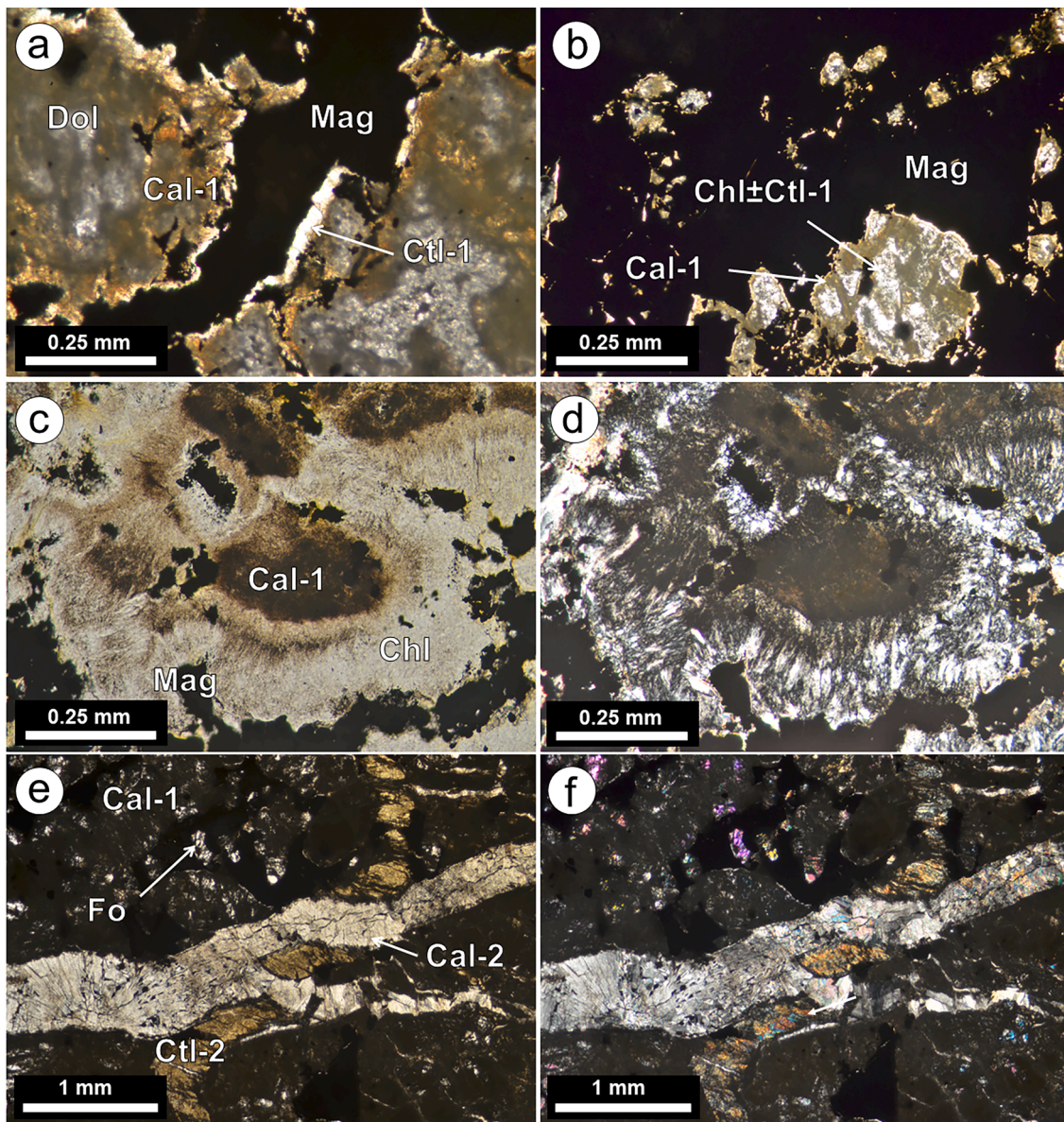


Fig. 5. Photomicrographs of the Cal-Chl-Srp skarn from the San Manuel deposit. (a) Vein-like magnetite ore. Gray-colored dolomite is partially replaced by brownish, dust calcite forming the matrix. (b) Pod of semi-massive magnetite ore. Plane- (c) and crossed-polarized (d) light photomicrographs of typical carbonate replacement to chlorite from the Fo-Cal skarn. Plane- (e) and crossed-polarized (f) light photomicrographs of late calcite (Cal-2) crosscutting both carbonate matrix (Cal-1) and late chrysotile (Ctl-2). Note the occurrence of forsterite relicts. Cal-1: calcite-1; Dol: dolomite; Mag: magnetite; Chl: chlorite; Ctl-1: chrysotile-1; Cal-2: calcite-2; Fo: forsterite. Abbreviations from [Whitney and Evans \(2010\)](#).

(81.23–85.08 wt%) contents. Mag-1 also exhibit minor SiO_2 (<0.60 wt%), Al_2O_3 (0.19–0.62 wt%), and MnO (0.14–0.24 wt%) (Appendix E). In contrast, Mag-2 falls within the compositional field of magnetite exhibiting widely variable but significantly lower MgO (<3.94 wt%) contents, with higher FeO_{tot} (84.66–94.45 wt%), and similar but slightly higher SiO_2 (<0.98 wt%), Al_2O_3 (<0.85 wt%), and MnO (<0.35 wt%) than Mag-1 (Appendix E). Mag-3 displays lower MgO (<1.73 wt%), higher FeO_{tot} (86.57–93.36 wt%), and similar SiO_2 (<0.63 wt%) than the former Mag-1 and Mag-2. However, the most striking feature of Mag-3 is its elevated Al_2O_3 (<3.53 wt%) and TiO_2 (<3.96 wt%), consistent with the presence of minute spinel inclusions (Fig. 11; Appendix F), which were as avoided as possible in single-spot EPMA analyses. Mag-4 yields the lowest MgO (<0.77 wt%), Al_2O_3 (<0.83 wt%), and SiO_2 (<0.58 wt%) but the highest FeO_{tot} (89.22–94.16 wt%) (Appendix E). Other elements including Cr_2O_3 , CaO, ZnO, NiO, TiO_2 , V_2O_5 are below or marginally higher than the detection limit of EPMA in the analyzed

grains (except TiO_2 in Mag-3).

In-situ LA-ICP-MS results are consistent with the differences noted above (Fig. 13; Appendix G). Mag-1 ($n = 17$) and Mag-2 ($n = 51$) are similar in terms of Co, Zn, Ni, and Sn (average: 216 ppm, 130 ppm, 92 ppm, and 29 ppm, respectively in Mag-1, and 197 ppm, 161 ppm, 89 ppm, and 36 ppm, respectively in Mag-2), although Mag-1 has higher Mn (average: 1440 ppm), and lower Si, Ca, and Sr (average: 1052 ppm, 2833 ppm, and 12 ppm, respectively) than in Mag-2 (8204 ppm, 8980 ppm, and 49 ppm, respectively) (Fig. 13; Appendix H). The analyzed grains of Mag-3 ($n = 32$) exhibit lower Ca (below or marginally higher than the detection limit) Sr, Sn, and Ni (average: 2 ppm, 17 ppm, and 22 ppm, respectively) than former Mag-1 and Mag-2, but similar Co and Zn (average: 206 ppm, and 168 ppm, respectively). The most striking feature of Mag-3 is the highest Ti, V, and Ga (average: 5073 ppm, 368 ppm, and 20 ppm respectively) contents, consistently with single-spot EPMA results (Fig. 13; Appendix E). In the binary diagrams Ti vs. V,

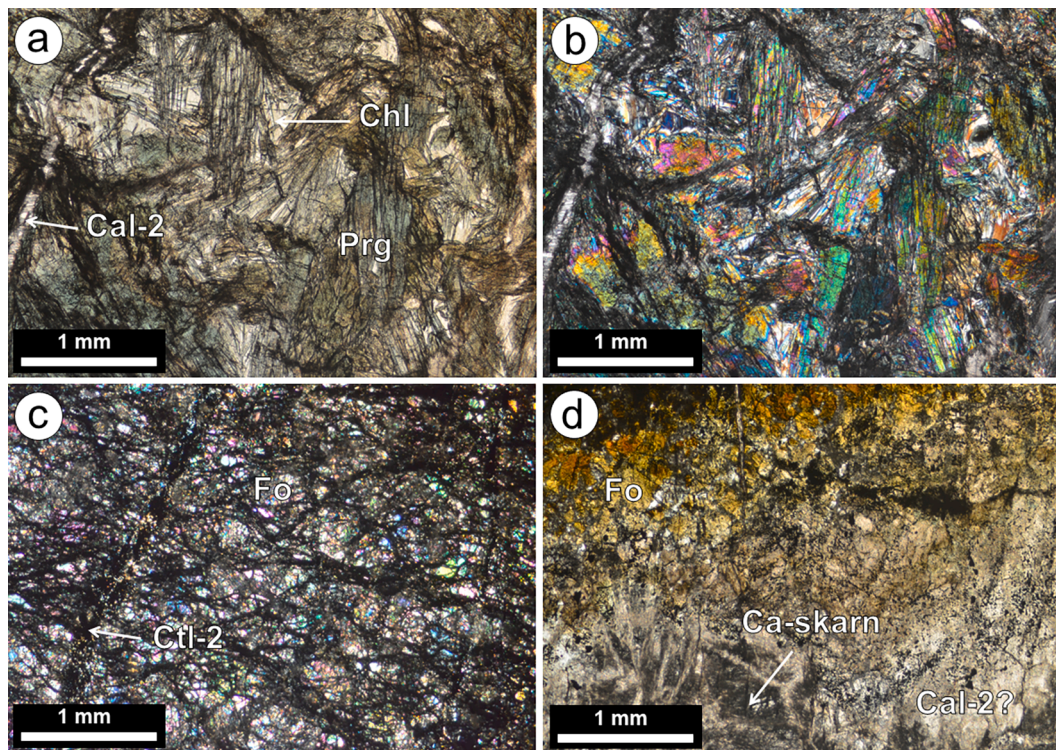


Fig. 6. Photomicrographs of the Ca-skarn zone from the San Manuel deposit. Plane- (a) and crossed-polarized (b) light photomicrographs of a pargasite-rich zone with minor white-colored chlorite. Late calcite (Cal-2) crosscutting this domain can be shown on the left part. (c) Forsterite-rich domain close to the Ca-skarn. (d) Limit between Ca-skarn and forsterite rich domain. This limit is composed of Si-rich yellow forsterite and white-colored calcite. Chl: chlorite; Cal-2: calcite-2; Prg: pargasite; Fo: forsterite; Ctl-2: chrysotile-2. Abbreviations from Whitney and Evans (2010).

Mineral	Before skarn	Prograde	Retrograde	Sulfide Stage	Ca-Skarn
Dolomite					
Forsterite					
Magnesioferrite (Mag-1)					
Magnetite-2					
Magnetite-3					
Calcite-1					
Chlorite					
Antigorite					
Chrysotile-1					
Magnetite-4					
Chrysotile-2					
Pyrite					
Chalcopyrite					
Calcite-2					
Pargasite					

Fig. 7. Mineral parageneses of the San Manuel iron skarn deposit.

and Al vs. Ga, they exhibit positive correlation respectively, suggesting that these elements behave similarly during skarn evolution (Appendix H). Finally, Mag-4 (n = 6) shows the lowest total trace element contents, with an average of 32 ppm Mn, 667 ppm Si, 2 ppm Zn, 12 ppm Co, 23

ppm Ni and < 1 ppm Sr (Fig. 13; Appendix H).

4.2.3. Solid mineral inclusions in magnesioferrite-magnetite

Mag-1 is virtually free of inclusions whereas Mag-2 exhibits pores

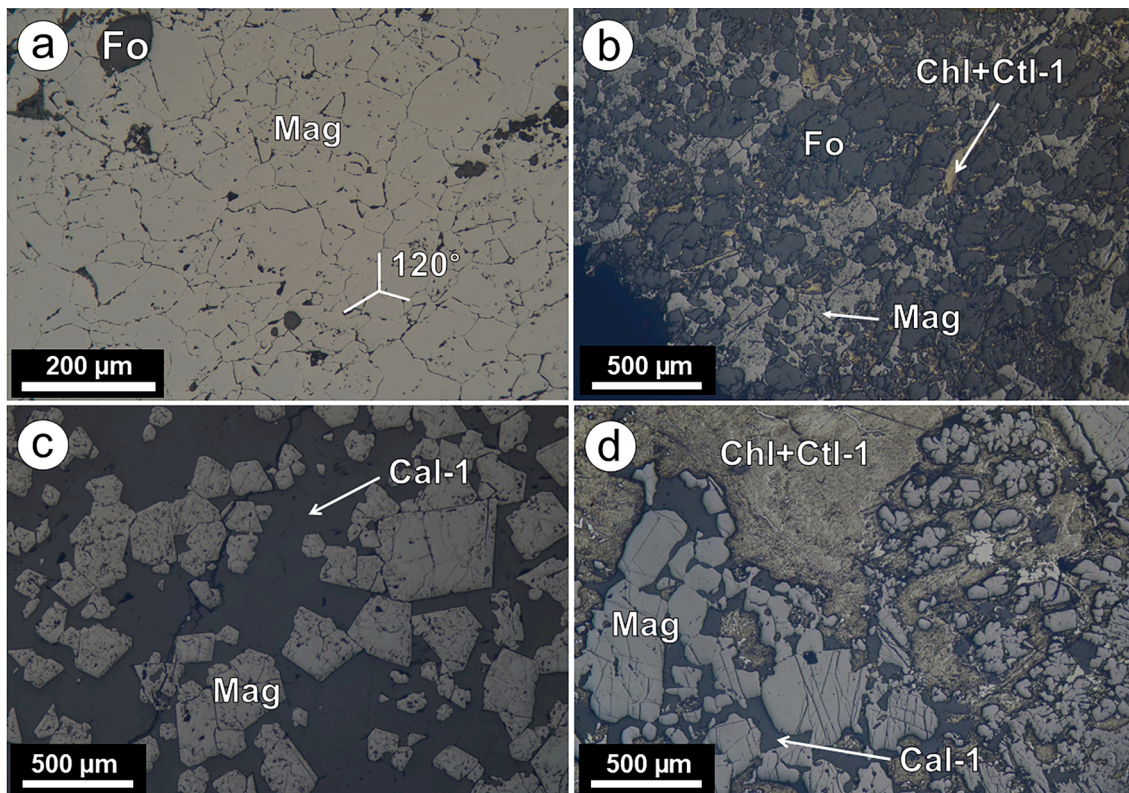


Fig. 8. Reflected light microphotographs of different magnetite textures of the ore zone from the San Manuel skarn. (a) Massive magnetite texture forming 120° triple junction. (b) Interstitial-to-forsterite semi-massive magnetite from the upper part of the ore zone. (c) Disseminated magnetite embedded in the host carbonatic rock from the lower part of the ore zone. (d) Semi-massive magnetite mineralization from the lower part of the ore zone embedded within the chlorite ± serpentine matrix. Note the presence of most calcite related to magnetite. Fo: forsterite; Mag: magnetite; Chl: chlorite; Ctl-1: chrysotile-1; Cal-1: calcite-1. Abbreviations from Whitney and Evans (2010).

filled by single or composite inclusions made up of forsterite ± calcite ± chlorite ± serpentine (Fig. 11c; Appendix F). Mag-3 has finely grained inclusions of spinel (<2 µm) with preferred orientation (Fig. 11f and i; Appendix F). In contrast, Mag-4 is free of inclusions. One Focused Ion Beam (FIB) thin foil (profile A-A' in Fig. 14a-b) was cut across an inclusion in Mag-2, which was previously identified employing Energy-dispersive X-Ray Spectroscopy (EDS) analysis using a Field Emission Scanning Electron Microscope (FE-SEM), as a complex compound with Al, Si, Mg, and Ca (Fig. 11c; Appendix F). The high-angle annular dark-field (HAADF) image of the cross-section revealed an almost triangular shape of this inclusion consisting of three different individuals (Fig. 14b). The TEM-EDS elemental mapping shows that the central portion of the inclusion is a Ca-rich mineral, while the outermost consists of two different Si-rich minerals, enriched in Mg and Al respectively (Fig. 14c-d). Selected area electron diffraction (SAED) patterns acquired at the contacts between the three members of the composite inclusion and host Mag-2 indicate that they are randomly oriented one each other and with the host Mag-2 (Fig. 14e-h). The SAED patterns of the central portion of the Ca-rich inclusion yield measured d-spacing of 1.94 Å (Fig. 14f), matching the ideal d-spacing 1.93 Å (024) of calcite (Table 2; Graf, 1961). The Mg-rich domain at the edge of the inclusion was identified as forsterite partially altered to serpentine (Fig. 14g-h), according to two different measured d-spacings: 3.55 Å, close to ideal 3.50 Å (111), and 4.76 Å corresponding to the cell parameter (100) (Wechsler et al. 1984), as well as single-spot Analytical Electron Microscopy (AEM) analysis $\text{Si}_{1.05}(\text{Mg}_{1.81}\text{Fe}_{0.08})_{1.88}\text{O}_4$ (Table 2). The surrounding Al-rich part is identified as chlorite by single-spot AEM with the following structural formula: $(\text{Si}_{2.90}\text{Al}_{1.10})_{4.00}(\text{Mg}_{5.01}\text{Al}_{0.50}\text{Fe}_{0.78})_{6.30}\text{O}_{10}\text{OH}_8$ (Table 2). In addition, the High-Resolution Transmission Electron Microscopy (HRTEM) investigations carried out at the deepest region of this FIB thin-foil reveal a very homogenous

distribution of Fe in Mag-2, as well as the presence of elongated and oriented nano-sized particles enriched in Al and Mg, which were not identified in the BSE image, acquired using FE-SEM on the surface of the polished thin section (Fig. 14c-d). Although d-spacing is not provided in the figure, these particles with preferred orientation were identified as spinel.

A second thin-foil (profile B-B' in Fig. 14a) crosscutting large inclusion within Mag-2 was also studied. This thin-foil intersected a more complex inclusion consisting of an intergrowth of calcite and forsterite partially replaced by serpentine (Fig. 14a-m). Calcite was identified by two distinctly oriented domains forming part of the same crystal, i.e., d-spacings 2.83 Å and 2.26 Å (Fig. 14l) corresponding to the ideal 2.84 Å (006) and 2.28 Å (113) as defined by Graf (1961). Identification of forsterite was made by its measured d-spacing 3.59 Å (Fig. 14m) corresponding to (111) (Nord et al. 1982) and by single-spot TEM-EDS analysis: $\text{Si}_{1.00}(\text{Mg}_{1.96}\text{Fe}_{0.05})_{2.01}\text{O}_4$ (Table 2). The basal orientation of serpentine in the thin-foil did not allow for accurate measuring of the d-spacing (see diffuse rings in Fig. 14m, although single-spot AEM analysis yielded a composition close to $(\text{Si}_{0.92}\text{Al}_{0.08})_{2.00}(\text{Mg}_{1.54}\text{Al}_{0.22}\text{Fe}_{0.15})_{1.91}\text{O}_5\text{OH}_4$. A striking feature of this thin-foil is the presence of minute nanometer-sized (<100 nm) crystals of the Zn-rich spinel gahnite with measured d-spacings of 1.83 Å, 2.43 Å, and 2.85 Å, corresponding to (331), (311), and (220) of Popović et al. (2009) having same orientation than the host Mag-3 (Fig. 14k and n-o). Single-spot AEM analysis of two of the largest grains yielded $\text{Zn}_{1.24}\text{Al}_{1.84}\text{O}_4$ and $\text{Zn}_{1.38}\text{Al}_{1.74}\text{O}_4$ as the structural formula (Table 2).

The third thin-foil performed in this study sampled the contact between spinel-bearing Mag-3 core and inclusion-free Mag-4 rims (Fig. 15a). The inspection of the sampled area using a High-Resolution Transmission Electron Microscopy (HRTEM) confirmed the presence of spinel inclusions at depth (Fig. 15). These particles lack Fe and are

Table 1
Samples of the skarn deposit investigated in this study.

Sample	Skarn zone	Mineralization	Mineral assemblage	
			Gangue	Ore
SM-1	Fo-Cal skarn	Disseminated	Dol ± Cal ± Srp	Mag ± Py ± Ccp
SM-11	Massive ore	Massive	Cal + Srp ± Dol	Mag
SM-13	Ca-skarn	–	Prg + Chl ± Fo	–
SM-18	Ca-skarn	–	Prg + Chl ± Fo	–
SM-2-1	Fo-Cal skarn	Disseminated	Dol	Mag
SM-2-2	Fo-Cal skarn	Disseminated	Dol	Mag ± Py
SM-25	Fo-Cal skarn	Semimassive	Chl ± Srp ± Cal	Mag ± Ccp ± Py
SM-26	Migmatite	Disseminated	Qtz + Mv ± Fo	Gr + Py ± Hem
SM-28	Cal-Chl-Srp skarn	Massive	Chl ± Srp ± Cal	Mag
SM-3	Cal-Chl-Srp skarn	Massive	Dol ± Srp	Mag
SM-30-1	Fo-Cal skarn	Disseminated	Dol ± Cal ± Fo	Mag
SM-30-2	Fo-Cal skarn	Disseminated	Dol ± Cal ± Fo	Mag
SM-32-1	Fo-Cal skarn	Semimassive-massive	Dol ± Cal ± Fo	Mag ± Hem
SM-32-2	Fo-Cal skarn	Semimassive-massive	Fo + Dol ± Srp	Mag ± Hem
SM-33	Cal-Chl-Srp skarn	Disseminated	Dol ± Srp ± Chl ± Cal	Mag ± Hem
SM-34	Massive ore	Massive	Fo ± Cal	Mag
SM-35	Fo-Cal skarn	Disseminated	Fo ± Cal	Mag ± Py
SM-36	Fo-Cal skarn	Semimassive-massive	Fo ± Dol ± Cal	Mag
SM-37	Cal-Chl-Srp skarn	SemiMassive	Srp ± Cal ± Chl	Mag ± Py ± Ccp
SM-39	Massive ore	Massive	Dol + Cal ± Srp ± Chl ± Fo	Mag
SM-43	Fo-Cal skarn	Disseminated	Fo + Dol ± Cal	Mag, Hem
SM-47	Massive ore	Semimassive-massive	Dol + Cal ± Srp ± Chl ± Fo	Mag ± Hem
SM-48	Massive ore	Semimassive-massive	Dol ± Srp ± Chl ± Cal	Mag
SM-49	Fo-Cal skarn	Disseminated	Fo ± Srp ± Chl ± Cal	Mag
SM-4	Fo-Cal skarn	Massive	Fo ± Cal	Mag
SM-50	Massive ore	Massive	Srp ± Dol ± Cal	Mag
SM-51	Cal-Chl-Srp skarn	Semimassive	Srp + Chl + Cal	Mag ± Py
SM-7	Cal-Chl-Srp skarn	Semimassive	Chl + Cal ± Srp	Mag, Hem
SM-8	Fo-Cal skarn	Disseminated	Dol + Cal ± Fo	Mag + Hem ± Py
SM-9	Massive ore	Massive	Srp ± Chl	Mag

very small in length (<2 μm) and thickness (<200 nm). They are preferentially oriented in the host Mag-3 along the common (1 1 1) plane (see corresponding d-spacings in Fig. 15 f-h and Table 2. Single-spot AEM analysis of spinel (n = 14) yields structural formula ranging from Mg_{0.84-96}Al_{2.02-2.10}O₄.

4.2.4. Microstructure of magnetite

Two EBSD maps were performed on selected areas from a massive sample (i.e., SM-28) consisting of Mag-3 cores rimmed by Mag-4 with a polygonal microstructure forming 120° triple junctions, (Fig. 16a-c).

The band contrast and EBSD colored maps of this sample reveal the coexistence of large irregular grains having appreciable internal crystal bending (rectangles A1 to A5 in Fig. 16e-g) with grains free of internal deformation as well as several small grains located at triple junctions (dashed circles in Fig. 16f-g). It is worth noting the presence of a small magnetite grain forming lamellar twins (rectangle B1 in Fig. 16e). The inverse pole figure acquired in 3D-space reference X₀, Y₀, and Z₀ shows no common orientation of these three types of grains (Fig. 16d). In this sample characterized by a polygonal microstructure, the orientation

data obtained from all grains analyzed, display near-random to very weak patterns of bulk crystallographic preferred orientation (CPO) with numerous orientation maxima at (1 0 0), (1 1 0), and (1 1 1) (Fig. 16d and h). The intracrystalline deformation observed in some of the largest grains (rectangles A1 to A5 in Fig. 16e-g) is recorded by low misorientation angles (<2°; see profile A-A' in Fig. 16c), whereas the misorientation angles at grain boundaries yield peaks > 20° (profile B-B' in Fig. 16c). Nevertheless, these crystallographic subdomains within the grains are unrelated to the original core-to-rim zoning. Crystallographic continuity between core and rim is also suggested by the distribution of misorientation angles within the single grains (<2°) in most of the mapped grains indicating that the rim is not randomly oriented to the core.

5. Discussion

5.1. Genesis of Mag-1, Mag-2, and Mag-3

The observation of Mag-1 cores replaced to various extents by Mag-2, Mag-3, and Mag-4 (Figs. 10 and 11), clearly suggest variations of the conditions of the hydrothermal fluid during the evolution of the skarn (e.g., Dare et al. 2014; Nadoll et al. 2014; Hu et al. 2014).

As illustrated in Fig. 7, Mag-1 is cogenetic to forsterite, suggesting its precipitation from hydrothermal fluids at the early prograde stage, very likely from Mg leached from dolomite by the incoming hydrothermal fluids. A maximum temperature of 700 °C at 0.3 GPa was suggested for the forsterite formation in dolomitic marbles thermally overprinted during the crustal emplacement of the Ronda peridotite (Mazzoli et al. 2013). These P-T conditions are consistent with those estimated for the processes of dehydration and subsequent anatexis that have produced the migmatites and granitic dyke swarms found in the crustal footwall of the Ronda peridotites (i.e., 600–750 °C at ~ 0.3 GPa; Cuevas et al. 2006; Acosta-Vigil et al. 2014). These granitic rocks postdate the latest metamorphic event recorded in the ultramafic body, which occurred at conditions 800–900 °C and 1 GPa (obtained for the aluminous mafic rocks alternating with peridotites and sampled near the marbles section studied in this work; Morishita et al. 2001).

Mag-1 is systematically rimmed by porous Mag-2 in the Fo-Cal skarn, which shows irregular sharp contacts with Mag-1. This suggests Mag-1 replacement via coupled dissolution-precipitation (DRP) processes (Hu et al. 2014, Hu et al., 2015; Zhang et al. 2020) during infiltration of hydrothermal fluids at increasing fluid/rock ratio. HRTEM observations evidence the presence of composite forsterite-calcite inclusions in Mag-2 which indeed indicate a prograde-related origin of Mag-2. These inclusions were replaced to various extents by serpentine and/or chlorite (Fig. 14a-j) suggesting subsequent overprinting of Mag-2 by late, cooler hydrothermal fluids during the retrograde stage.

Mag-3 exhibit high Al, Ti, V, and Ga contents indicating that these components increased and/or become saturated in the solution, especially in lower zones of the skarn, close to the fluid source, where the fluid/rock ratio was higher and thus Mag-3 replaced completely both Mag-1 and Mag-2. As marked by sharp and irregular contacts between Mag-3 and former magnetite the replacement also occurred via DRP processes. HRTEM observations revealed the presence of oriented spinel inclusions within Mag-3 along the common (1 1 1) plane (Fig. 15a-h). TEM-EDS elemental maps and single-spot compositions acquired for these domains indicate that most of these are Mg- and Al-bearing pure spinel (Fig. 15c-d). Although Ti is homogeneously distributed within magnetite, it is concentrated in the spinel boundaries to a greater extent (Fig. 15i-j). This could explain wide TiO₂ variations detected in Mag-3 employing EPMA (Appendix E) and LA-ICP-MS (Appendix G). Accordingly, Al and Mg in the original Mag-3 were preferentially included in spinel during oxy-exsolution, whereas Fe and most Ti remained in the precursor Mag-3. Quantitative LA-ICP-MS single-spot analysis of inclusion-free zones of Mag-3 (Appendix G) indicates up to ~ 3.5 wt% of Al₂O₃, which is a much higher concentration than previously reported in

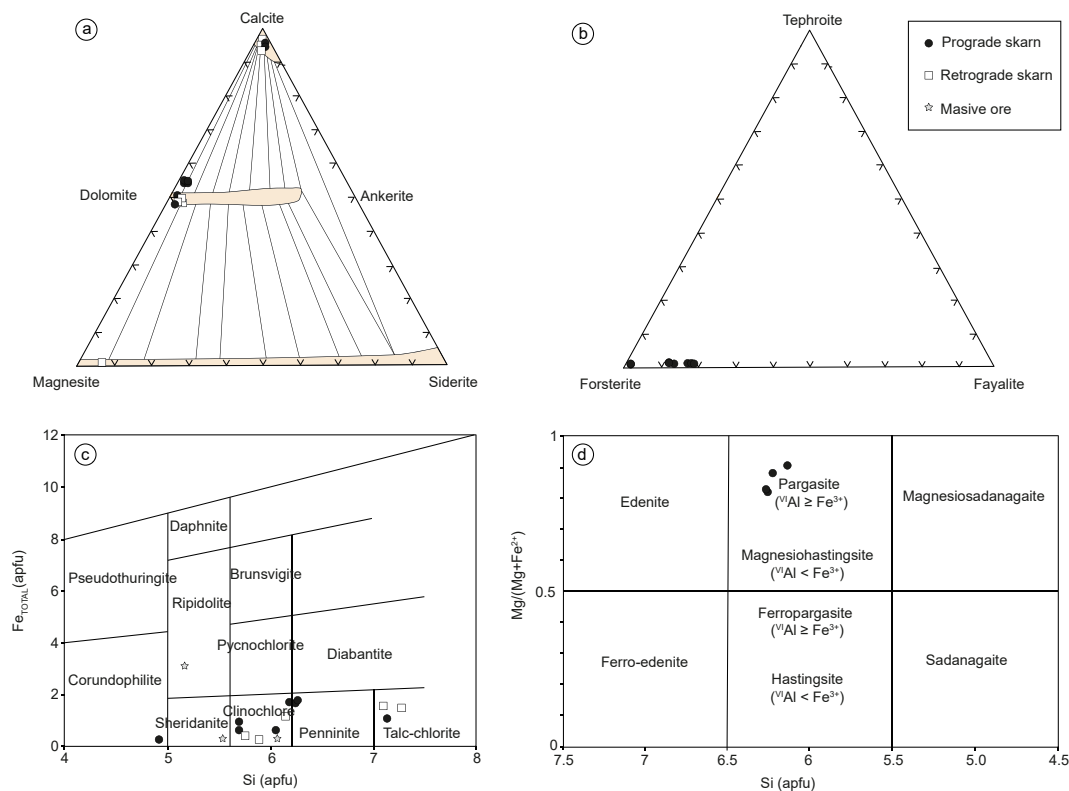


Fig. 9. Plotted EPMA results of the main skarn minerals. (a) Ternary diagram for Fe–Mg–Ca carbonates at 750 K and 1 bar pressure, using the approach of McSwiggen (1993a) and McSwiggen (1993b). (b) Forsterite composition on a forsterite–fayalite–Mn–olivine ternary plot. (c) Chlorite classification diagram from Hey (1954). (d) Amphibole classification diagram according to Leake et al., (2004) including analyzed minerals from the Ca-skarn. The diagram is applied to amphiboles where $Ca_B > 1.50$; $(Na + K)_A > 0.5$.

hydrothermal magnetite containing similar exsolutions from other Mg-skarn (up to 0.87 wt% Al_2O_3 in the Forsyth, Canada; up to 0.80 wt% Al_2O_3 in the Iron Crown, Canada; up to 1.15 wt% Al_2O_3 in the Chengao, China; up to 0.85 wt% Al_2O_3 in the Marmoration, Canada; and up to 1.20 wt% Al_2O_3 in the Daye deposits, China; Hu et al. 2015 and references therein).

Previous experimental (Lehmann and Roux, 1986; Sack and Ghiorso 1991a, b; Lindsley 1991; Rapp et al. 2010) and empirical (e.g., Dupuis and Beaudoin 2011; Hu et al. 2015; Ivanyuk et al. 2016, 2017) studies have shown that the solubility of Al in hydrothermal magnetite is strongly dependent on the temperature within the fO_2 conditions of the fayalite-magnetite-quartz buffer (FMQ). In particular, Sack and Ghiorso (1991a, b) defined the existence of miscibility gaps along the $MgFe_{1-x}Al_xFe_{2-x}$ exchange vector for Cr-free spinel (i.e., spinel-magnesioferrite) within the wide range of temperatures of $< 700^\circ$ to 1025° C. The projection of the pure composition of the spinel exsolution analyzed here (determined by HRTEM) and their host Mag-3 (determined by EPMA) in the Fe^{3+} and Fe^{2+} diagram calibrated by Sack and Ghiorso (1991b) suggest temperatures of spinel-magnetite exsolution in our samples below 700° C (Fig. 17a). These temperatures are similar to those (700 – 650° C) obtained by applying the calculated miscibility gaps for the Fe^{2+} and Mg^{2+} binaries of the spinel prism (i.e., spinel-magnesioferrite) (Fig. 8 in Sack and Ghiorso 1991a). To this approach, we assumed that only Al (and not Fe^{3+}) was partitioned into spinel during oxy-exsolution. Moreover, the molar fraction (x-axis; Fig. 8 in Sack and Ghiorso 1991a) is considered equivalent to calculated volume proportion (spinel/magnetite = 11.6–10.13%; Appendix A). Therefore, estimated spinel-magnetite exsolution temperatures of $< 700^\circ$ C could be considered as a minimum formation temperature of the Mag-3. Considering the uncertainties inherited to the applied approach, these temperatures are consistent with those estimated for the prograde stage fluids (i.e., 600 – 700° C; see Mazzoli et al. 2013, Acosta-Vigil et al.

2014), as well as temperatures suggested for the exsolution of similar spinel inclusions in hydrothermal magnetites elsewhere (e.g., Ivanyuk et al. 2016, 2017). In our study case, spinel-magnetite exsolutions in the Mag-3 should mark the minimum temperature of the prograde stage (i.e., $< 700^\circ$ C). On the other hand, chlorite geothermometry shows temperatures ranging from 267 to 435° C (Appendix I) indicating that retrogradation persisted, at least, to these temperatures.

5.2. Syn-deformational Mag-4 rims

Massive samples exhibit polygonal microstructure consisting of coarse-grained, internally deformed grains and smaller-faced grains at triple junctions (Fig. 16a-c). This type of microstructure is usually produced in Fe-Ti-Cr oxides when crystal-plastic deformation is accommodated by grain boundary migration and subsequent recrystallization (Rosière et al. 2001; Ávila et al. 2015; Ghosh and Konar, 2012; Ghosh et al. 2014, Ghosh et al., 2017; Satsukawa et al. 2015; González-Jiménez et al. 2018). These microstructures have also been reported in other skarn-related hydrothermal magnetites and interpreted as reflecting: (1) high-temperature annealing in a closed system (e.g., Coibanu and Cook, 2004), (2) and/or fluid-assisted replacement in an open system (e.g., Hu et al. 2015; Zhang et al. 2020). However, none of the cited works paid attention to the potential effects of deformation.

Some of the large grains analyzed here exhibit intra-crystalline bending and slight internal misorientation (e.g., grains enclosed within rectangles A1-A5 in Fig. 16e-g), which indeed is consistent with deformation. Thus, if annealing took place in a high-temperature closed system but under deformation, one could expect that upon progressive deformation of the pre-existing larger crystals, dislocations in the hosting magnetite crystal would migrate and accumulate to discrete zones, giving rise to the formation of subgrain boundaries, and in the ultimate instance, to grains (e.g., Satsukawa et al. 2015; González-Jiménez et al.

Table 2

Indexed SAED and HREM d-spacing values for minerals shown in Figs. 14 and 15. *d-spacing deviations ascribed to Fe content in forsterite that distorts the structure ($d_{\text{forsterite}} = 3.56\text{\AA}$).

Calculated mineral formula by analytical electron microscopy (AEM)	Not measured	Not measured	Si _{1.05} (Mg _{1.81} Fe _{0.08}) _{1.88} O ₄	Not measured	Not measured	Not measured	Not measured	Si _{1.00} (Mg _{1.96} Fe _{0.05}) _{2.01} O ₄	(Mg _{0.84-96} Al _{2.02-2.10}) _{2.94-2.97} O ₄	(Mg _{0.84-96} Al _{2.02-2.10}) _{2.94-2.97} O ₄	Not measured	Not measured	(Zn _{1.38} Al _{1.74}) _{3.12} O ₄	Not measured	Not measured	(Zn _{1.24} Al _{1.84}) _{3.08} O ₄	Not measured	Not measured
Spinel									4.67	4.67								
theoretical d-spacing																		
Spinel									4.68	4.66								
measured SAED d-spacing																		
Gahnite													2.86			2.44	1.85	
theoretical d-spacing																		
Gahnite													2.85			2.43		
measured HREM d-spacing																		
Gahnite																	1.83	
measured SAED d-spacing																		
Forsterite			4.76					3.50	3.50									
theoretical d-spacing																		
Forsterite			4.76					3.55	3.59									
measured SAED d-spacing																		
Magnetite				4.84	4.84	4.84						2.96		2.42	2.42			1.71
theoretical d-spacing																		
Magnetite				4.85	4.84	4.83									2.45			1.79
measured SAED d-spacing																		
Magnetite												2.96		2.42				
measured HREM d-spacing																		
Calcite	2.84	1.93																2.28
theoretical d-spacing																		
Calcite		1.94																
measured SAED d-spacing																		
Calcite	2.83																	2.26
measured HREM d-spacing																		
(hkl)	006	024	100	111							113	220		222		311	331	422

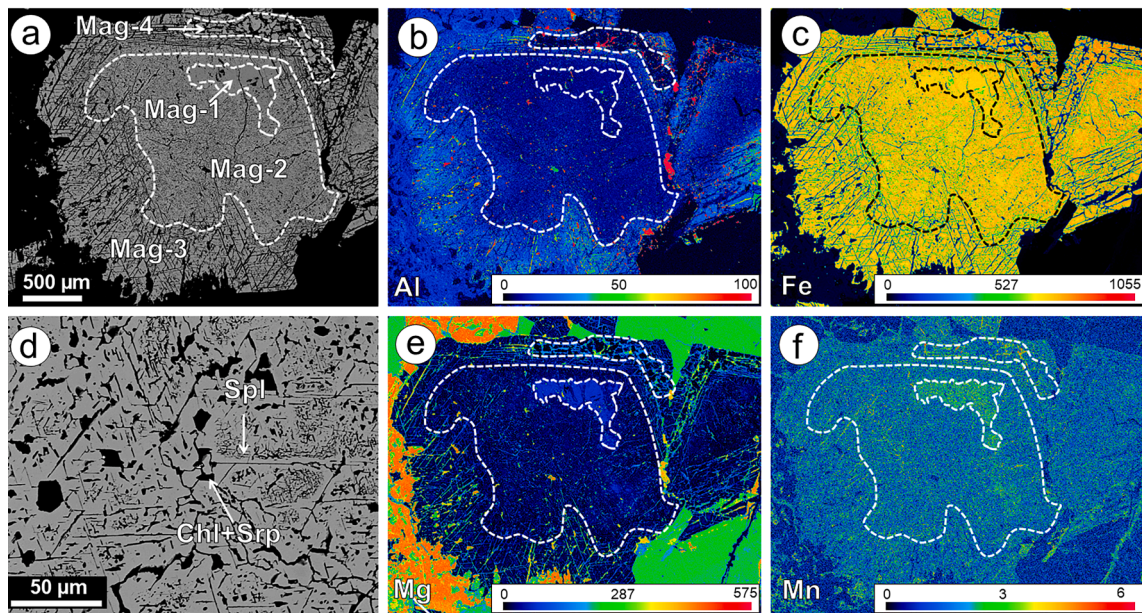


Fig. 10. (a) Backscattered electron images of zoned magnetite preserving all magnetite generations reported in this study (i.e., Mag-1 to Mag-4). Wavelength-dispersive spectrometry (WDS) X-ray elemental maps of zoned magnetite (b-c and e-f). Color scale bars show element concentrations in X-ray intensity (counts per millisecond per microampere). Note the positive correlation between Mg and Mg contents. (d) Backscattered electron detailed image of inclusions in zoned magnetite. Mag: magnetite; Spl: spinel; Chl: chlorite; Srp: serpentine. Abbreviations from [Whitney and Evans \(2010\)](#).

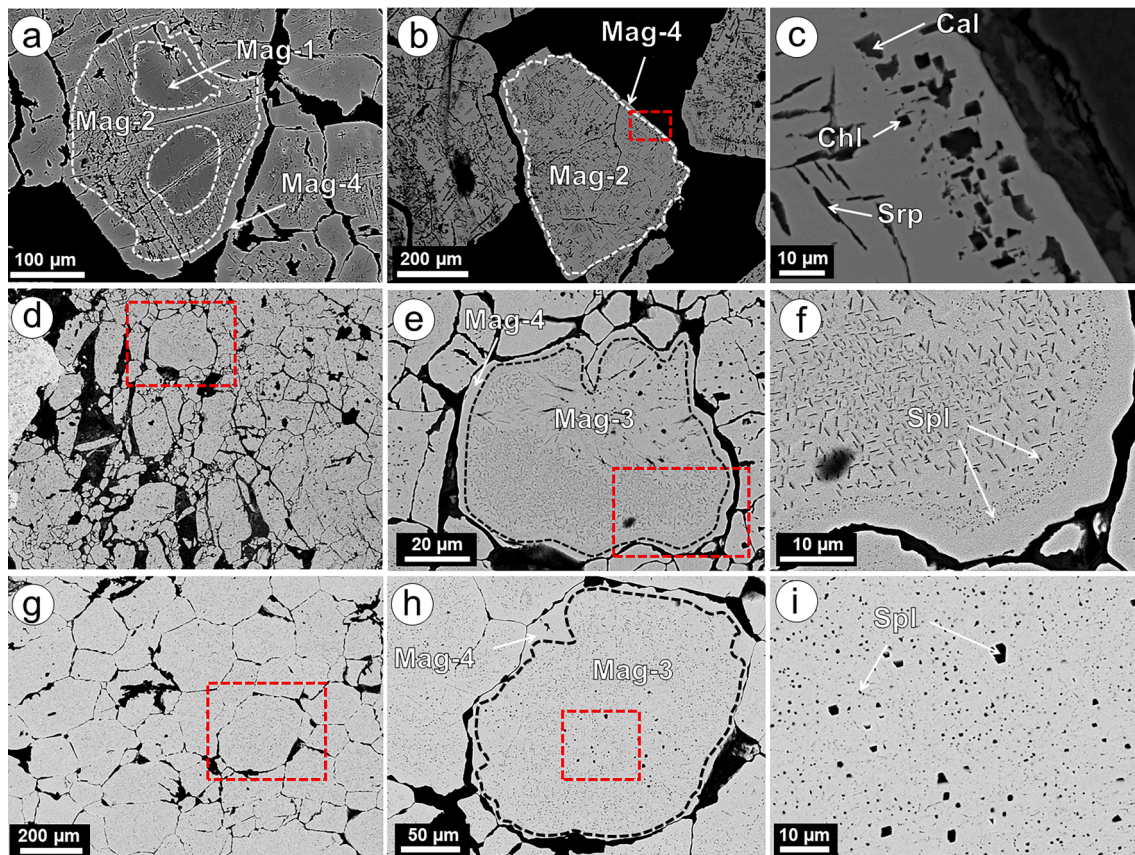


Fig. 11. Backscattered electron images acquired using FE-SEM of different types of zoned magnetite and their hosted inclusions. (a-c) Disseminated magnetite zoned grains from the Fo-Cal skarn (sample SM-2-2 in [Fig. 3a](#)). (d-f) Pod of semi-massive spinel-rich magnetite exhibiting polygonal textures (sample SM-25 in [Fig. 3a](#)). (g-i) Massive polygonal spinel-rich magnetite from the Cal-Chl-Srp skarn (sample SM-28 in [Fig. 3a](#)).

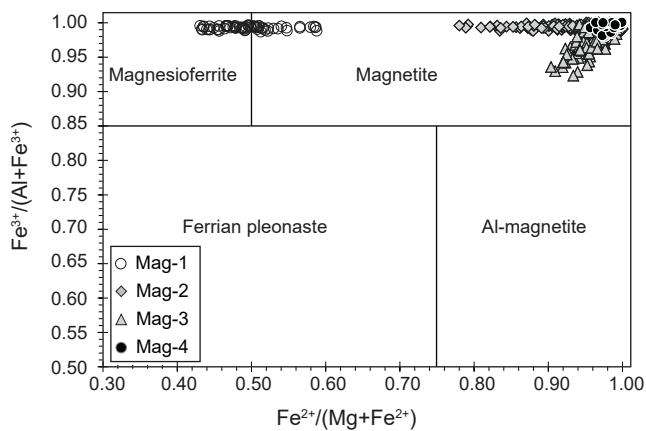


Fig. 12. Compositional variation of the zoned magnetite-magnetite from the San Manuel Mg skarn deposit. Cores of Mag-1 overlap the fields of magnesioferrite and magnetite. An overall Fe-enrichment trend is observed from Mag-1 to Mag-4.

2018). However, these grains are not the rule in our samples. Rather most of the grains analyzed here display core-to-rim crystallographic continuity. The observation that Mag-3 cores exhibit irregular shapes but still preserve oriented spinel exsolutions, and that their trace element composition is distinctively different to that of Mag-4 rims (which lacks solid inclusions and is significantly richer in Fe), is indeed more consistent with fluid-assisted replacement of pre-existing Mag-3 cores by Mag-4 in an open system.

Strain-free grains show distinct crystallographic orientation and misorientation degrees > 20° between different grains (Fig. 16e-g), supporting the idea that deformation was still active during crystal growth of Mag-4 rims. The initial stage of high-angle grain boundary formation by grain rotation may have been accompanied by grain

growth along newly-formed grain boundaries, as is suggested by the lack of substructures in the newly-forming Mag-4 (Fig. 16a-g). The nearly cubic morphologies shown by some of the newly-formed strain-free rims of Mag-4, and their mutual high angle (120°) triple junction boundaries displaying both finer and neighbor-finer dispositions and polygonal habits, indicate that the growth morphology of the boundaries of these grains was controlled by interfacial energy of the cubic crystals (Halfpenny et al. 2006). The presence of deformation-related lamellar twins within some faceted grains (rectangle B1 in Fig. 16e) is also consistent with deformation. Such deformational structures indicate a recovery process once the internal strain energy was accommodated by deformation of the entire aggregate.

On the other hand, the proposed mechanism of dynamic fluid-assisted replacement of pre-existing magnetite is also consistent with the observation that many of the triple junctions exhibited by the strain-free grains are frequently joined by chlorite and/or serpentine (Fig. 16a). This suggests solute escape from the high-angle migrating front during dynamic crystal growth of Mag-4. Thus, the observation that Mag-4 rims are almost inclusion-free suggests that the solid mineral inclusions, if originally present in the Mag-3, were dissolved and/or expelled out to intergranular positions during grain boundary migration (e.g., Satsukawa et al. 2015; González-Jiménez et al. 2018). These silicates may have acted as cushions that softened the inter-crystalline deformation, thus explaining why subgrain boundaries are not the rule in our samples. However, the formation of these recovery microstructures, which usually involves the removal of the newly-formed silicates in the most deformed grains, is not only associated with high strain but also requires relatively high-temperature conditions (e.g., Coibanu and Cook, 2004). Previous studies from hydrothermal systems and skarns suggest recrystallization of magnetite at > 550 °C (Rosière et al. 2001; Coibanu and Cook 2005). Interestingly, microfibrils preserved in marbles of contact metamorphic aureole at the footwall of the Ronda peridotites indicate that deformation associated with crustal emplacement of these ultramafic rocks was still active until 510 °C (Mazzoli et al. 2013).

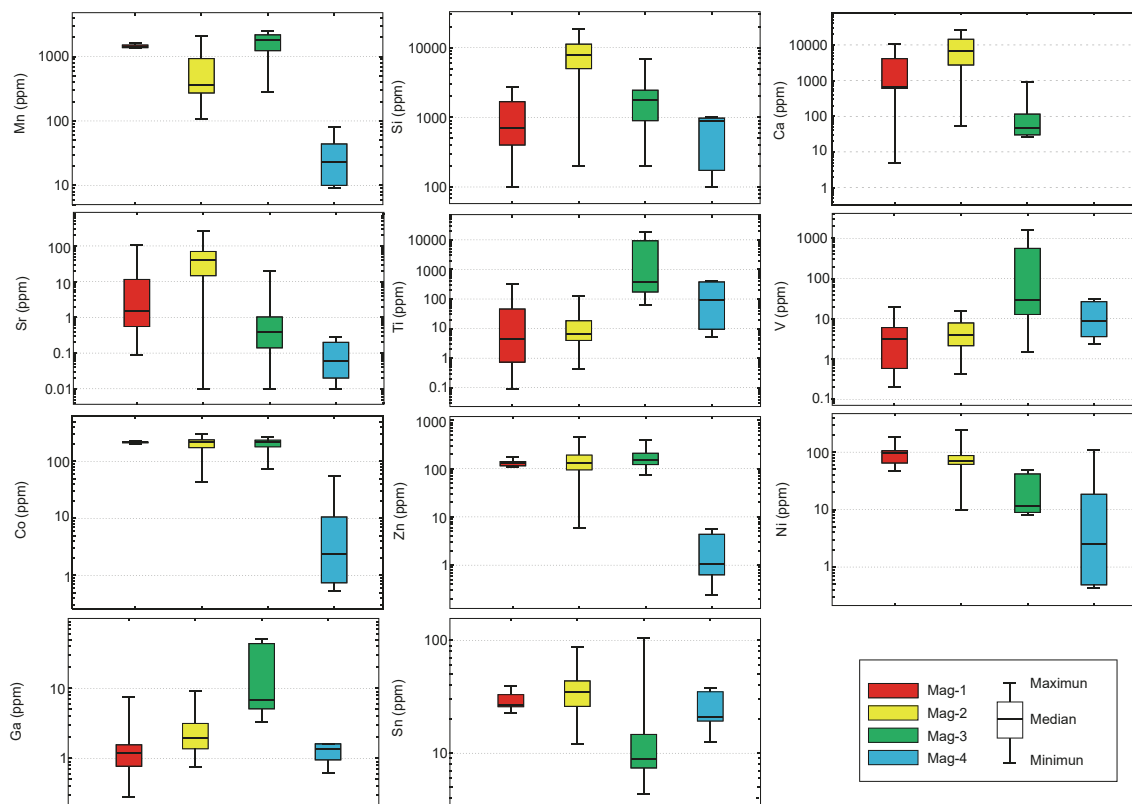


Fig. 13. Box and whisker plots showing the distribution of trace elements in the zoned magnetite grains from the San Manuel deposit.

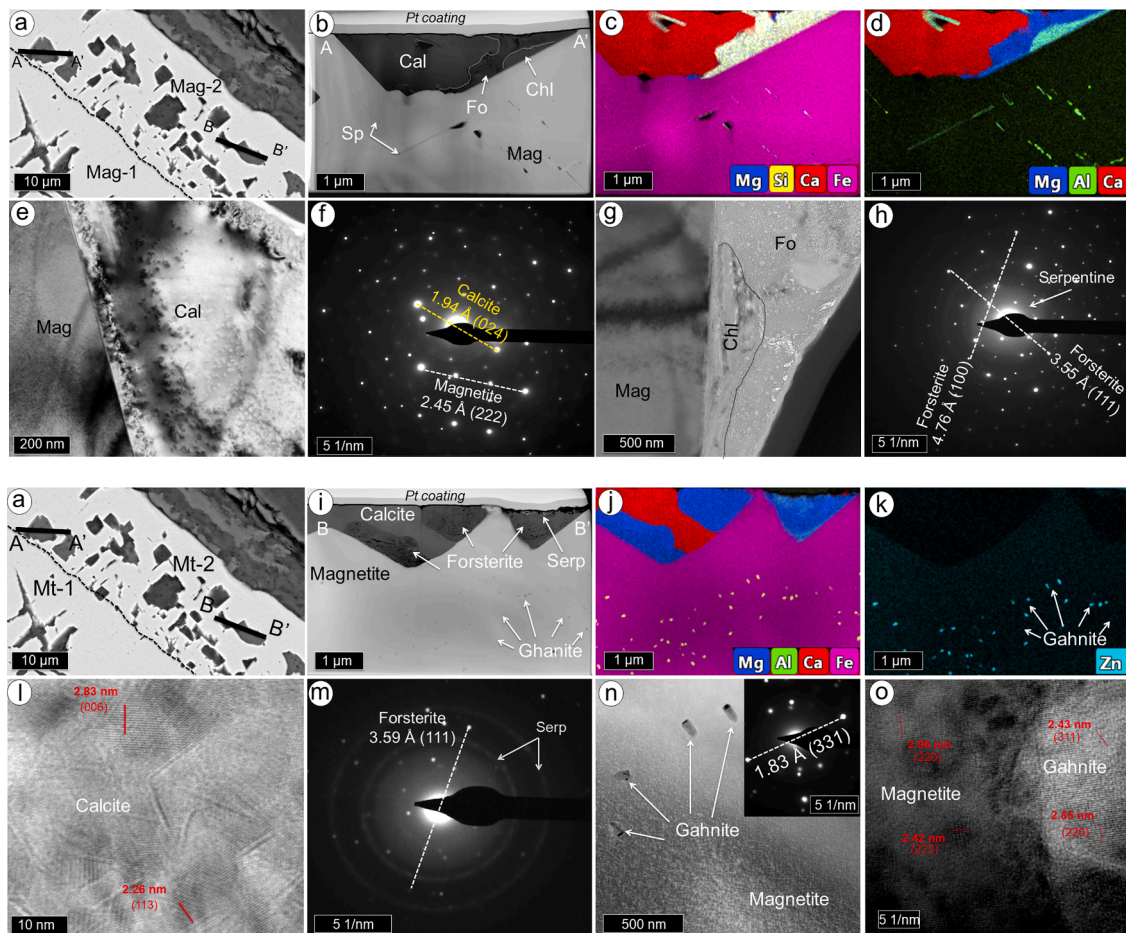


Fig. 14. (a) Backscattered electron image including location of thin-foil (A-A' and B-B') crosscutting inclusions in Mag-2. Sample SM-2-2. (b and i) HAADF scanning transmission electron microscopy (STEM) image of A-A' and B-B' thin foils, respectively (b) and B-B' thin-foil sampled. (c-d) and (j-k) TEM-EDS elemental maps acquired from the A-A' and B-B' thin-foil, respectively, included in Mag-2. SAED of the calcite-magnetite boundary (e-f), and forsterite (g-h) of the A-A' thin section. (l) High-magnification HRTEM image of calcite and corresponding SAED (m). (n) HRTEM image of gahnite inclusions in magnetite showing in (k). Inset: SAED of image (n). (o) High-magnification HRTEM image of gahnite inclusions showed in (n).

5.3. Geochemical fingerprints of the ore-forming fluids

Above, we suggested that during the early prograde stage Si-rich fluids reacted with dolomite to form Mg-rich minerals (i.e., forsterite and magnesioferrite) and residual calcite. However, these carbonatic rocks were not only enriched in Mg but also in Ca. In fact, in situ LA-ICP-MS analysis reveal that Mag-1 and Mag-2 are also enriched in Ca (2800 ppm, and ~ 9000 ppm on average respectively) relative to the other magnetite generations (<200 ppm on average) (Fig. 13); Appendix G), providing evidence of the effect exerted by the host rock in the hydrothermal fluid. The extent of this impact may be additionally estimated by using the discriminating plot (Mg + Mn) vs. (Si + Al)/(Mg + Mn) proposed by Hu et al. (2014) (Fig. 18a). In this diagram, the higher contribution of the carbonatic rock (and lower fluid/rock ratios) is related to higher (Mg + Mn) contents and lower (Si + Al)/(Mg + Mn) ratios. As expected, early-formed Mag-1 contains higher average (Mg + Mn) contents but lower (Si + Al)/(Mg + Mn) ratios than the secondary varieties (i.e., Mag-2, Mag-3, and Mag-4) (Fig. 18a).

Mag-3 contains much higher concentrations of Al₂O₃ (<4 wt%) and TiO₂ (<4 wt%) than early-formed Mag-1 (<0.62 wt% Al₂O₃ and < 0.07 wt% TiO₂) and its postdating Mag-4 (<0.83 wt% Al₂O₃ and 1.9 wt% TiO₂) (Fig. 18b; Appendix G). Consistently, Mag-3 contains exsolution

lamellae of spinel (Fig. 11). Single spot LA-ICP-MS analyses in areas free of these inclusions also show significantly higher contents of V in Mag-3 (~368 ppm in average) relative to Mag-1 and Mag-2 (~5 ppm) (Fig. 13; Appendix G). Previous studies indicate that depletion in V in magnetite may reflect an increase in *f*O₂ (Toplis and Corgne 2002; Richter et al. 2006; Acosta-Góngora et al. 2014; Nadoll et al. 2014, Nadoll et al., 2015; Sun et al. 2017) and/or temperature (Acosta-Góngora et al. 2014; Canil et al. 2016). (Al + Mn) vs. (Ti + V) diagram has been proposed as an indicator of magnetite formation temperature in hydrothermal systems (e.g., Nadoll et al. 2014; Sun et al. 2017). Fig. 18b shows that Mag-3 exhibits the highest (Al + Mn) vs. (Ti + V) contents supporting the fact that Mag-3 records the highest formation temperature. In fact, magnetite with high Ti, V, and Ga contents and similar texture to Mag-3 has been ascribed to high-temperature processes in hydrothermal systems (i.e., (Hu et al., 2020).

Trace elements also display variability in their contents among the different magnesioferrite-magnetite generations, suggesting that they acted as mobile elements (Fig. 13) (Dupuis and Beaudoin, 2011; Nadoll et al. 2014; Dare et al. 2014; Deditius et al. 2018). There is a continuous increase in the amount of Al, Ti, V, and Ga from Mag-1 to Mag-3. Contrary, Mag-1 and Mag-2 exhibit similar trace element composition, except for Si, Ca, and Sr, which could be related to forsterite + calcite

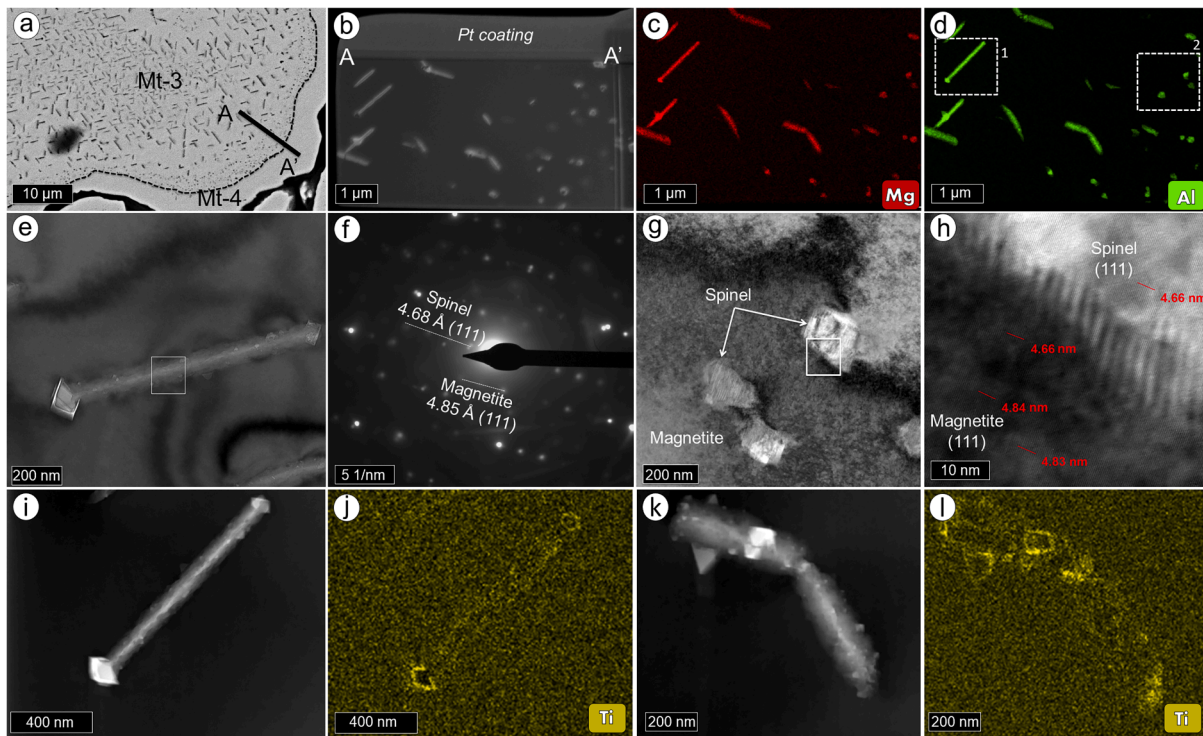


Fig. 15. (a) Backscattered electron image including the location of thin-foil (A-A') crosscutting the boundary between Mag-3 and Mag-4. Sample SM-25. (b) HAADF-STEM image of A-A' thin-foil. (c-d) TEM-EDS elemental maps acquired from A-A' thin foil. White-dashed rectangles 1 and 2 indicate the location of HRTEM images (e) and (g) respectively. (f) SAED of the spinel exsolution within magnetite corresponding to the white rectangle in (e). (h) HRTEM image of squared spinel inclusions in magnetite corresponding to the white square in (g). (i and h) HAADF-STEM image of spinel crystals showed in TEM-EDS elemental maps for Ti in (j) and (l) respectively.

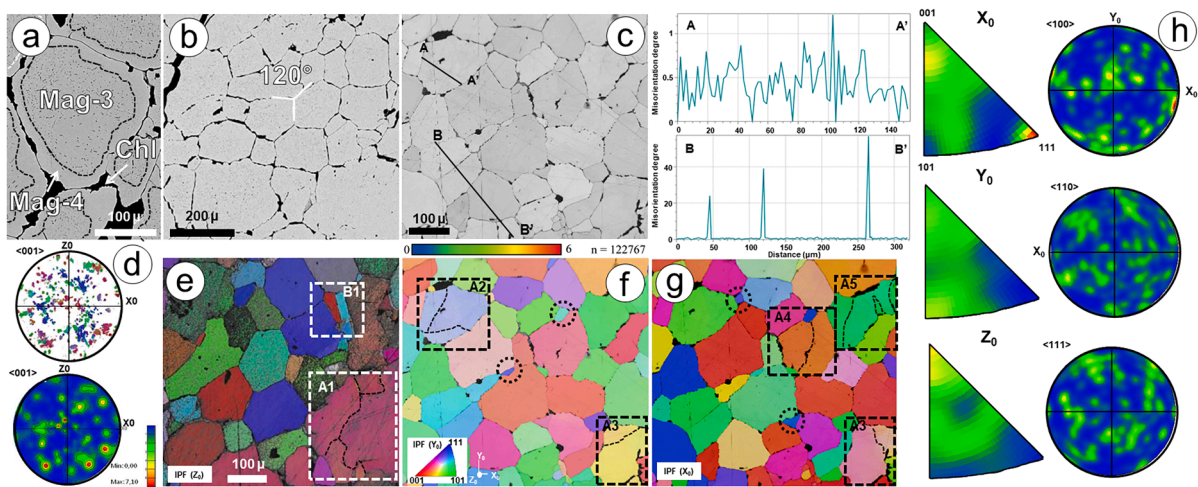


Fig. 16. Microstructure of massive magnetite ore from San Manuel deposit. (a) Backscattered electron image magnetite from massive sample showing spinel-rich Mag-3 core and free of inclusion Mag-4 rim. Note the occurrence of intergranular chlorite due to solute scape during recrystallization. (b) Backscattered electron images of massive recrystallized magnetite with 120° triple junction. (c) Backscattered electron image of massive magnetite and misorientation profiles (A-A', B-B'). Note the misorientation angles $> 20^\circ$ suggesting rotation processes. (d) Pole figure. (e-g) Color-coded EBSD map showing crystal orientation changes relative to the X, Y, and Z direction of the sample reference frame. Grains with internal crystal bending (dashed rectangles) coexist with free of deformation grains and small faceted grains at the triple junction (dashed circles). (h) Near-random to very weak patterns of CPO with numerous orientation maxima at (100), (110), and (111). Abbreviations from [Whitney and Evans \(2010\)](#).

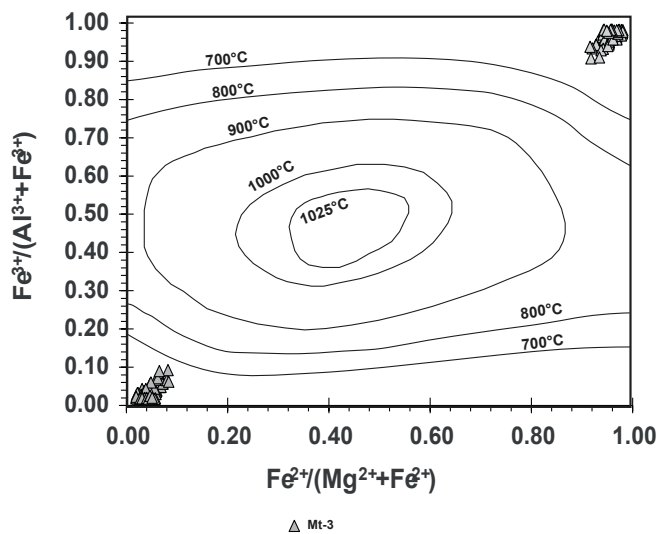


Fig. 17. Composition of the spinel and host magnetite plotted in a graphic showing the calculated miscibility gaps by Sack and Ghiorso (1991b) for (Fe, Mg) (Al, Fe³⁺)₂O₄ spinels at 700, 800, 900, 1000, 1025 °C (a), and the calculated miscibility gaps by Sack and Ghiorso (1991a) for the Fe²⁺ and Mg²⁺ binaries of the spinel prism, (Fe, Mg)(Al, Cr, Fe³⁺)₂O₄ (b). Both diagrams suggest a temperature of exsolution < 700 °C.

inclusions in Mag-2. There is almost no variation in terms of Co, Zn, and Ni from Mag-1 to Mag-3 (Fig. 13) indicating that chalcophile elements seemed to be immobile during DRP processes in the prograde stage. However, Sn is lower in Mag-3 which suggests *f*O₂ decrease, as Sn is redox-sensitive in magnetite (Carew 2004; Huang et al. 2019), in agreement with V increase in Mag-3.

Overall, Mag-4 shows the lowest total amount of trace elements (Fig. 13), consistent with fluid-assisted recrystallization that usually promotes the leaching of trace element contents (Hu et al. 2015; Zhang et al. 2020), as well as with lower temperatures that influence the incorporation of trace elements into magnetite (e.g., Nadoll et al., 2014; Deditius et al. 2018). This impoverishment is deeply marked in Zn, Co, and Ni which could be ascribed to the presence of co-precipitating sulfides (e.g., Hu et al. 2017; Sun et al. 2017). However, the Mag-4 in San Manuel skarn has no sulfide inclusions so this may indicate that these elements may be significantly mobile during the retrograde stage, contrary to the prograde stage. This indicates that their mobility is not temperature-dependent, but that changing conditions of the system allowed chalcophile elements to be mobile.

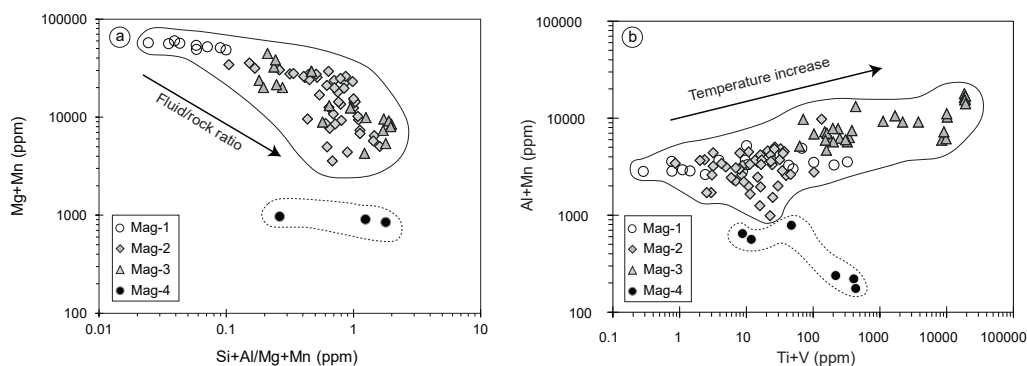


Fig. 18. Binary diagrams of LA-ICP-MS analysis of magnetite. There is a marked difference in composition between the retrograde-formed magnetite (Mag-4) and those crystals associated with prograde stages (Mag-1, Mag-2, and Mag-3). (a) (Mg + Mn) vs. (Si + Al)/(Mg + Mn) in ppm (Hu et al., 2014) showing the change of the magnetite composition from prograde-formed (Mg + Mn) rich, to retrograde-formed magnetite enriched in (Si + Al)/(Mg + Mn). (b) (Al + Mn) vs. (Ti + V) plot (in wt.%) for analyses of magnetite. Note that Mag-3 exhibits the highest values suggesting the highest formation temperature. Modified after Nadoll et al. (2014).

5.4. Genetic model

Fig. 19 shows a sketch illustrating the model we propose for the genesis of the San Manuel skarn deposit. The hot emplacement of Ronda peridotites over crustal rocks promoted dehydration and subsequent partial fusion of underlying crustal rocks of the Blanca unit. The model explains the variable zoning of magnesioferrite-magnetite crystals depending upon their distance to the potential fluid source (i.e., migmatite) (Fig. 19c). In the upper part of the skarn (i.e., Fo-Cal skarn) Mag-3 is absent and ore minerals are composed of remnant cores of Mag-1 rimmed by Mag-2, as well as Mag-4 rims (Fig. 11a; 1 in Fig. 19c). Contrary, Mag-3 is widespread in the lower part of the skarn (i.e., Cal-Chl-Srp) forming the magnetite cores rimmed by Mag-4 (3 in Fig. 19c). This heterogeneous distribution of the magnetite zoning along the skarn suggests that the fluid/rock ratio was not high enough in the Fo + Cal skarn to promote the full replacement of the preexisting Mag-1 and Mag-2, owing to the long distance to the fluid source. In contrast, the proximity of the Cal-Chl-Srp skarn to migmatite, promoted, at a higher fluid/rock ratio, the complete replacement of Mag-1 and Mag-2 to Mag-3. This would also explain why grains displaying a complete sequence of zoning (2 in Fig. 19c) are found in the middle of the skarn sequence.

During the prograde stage, the relatively hot hydrothermal fluid infiltrated the dolomitic rocks while forming prograde Mg-rich minerals (i.e., forsterite and magnesioferrite) (Fig. 19a). At this stage, Mag-1 would be the unique Fe-oxide variety dominating the whole skarn sequence (T1 in Fig. 19d), formed at around 600–700 °C as estimated above. Different pulses of hydrothermal fluids at increasing temperature and fluid/rock ratio may have promoted the disequilibrium with Mag-1 to form Mag-2, very likely involving DRP (T2 in Fig. 19d). During the prograde stage evolution, the solution became Al- and Ti-enriched and/or oversaturated, and reacted with already formed iron ores leading to the replacement of Mag-1 and Mag-2 to Mag-3 in various extents (T3 in Fig. 19d). This replacement may have been promoted by decreasing *f*O₂ now fingerprinted by the decrease of Sn and increase of V recorded in Mag-3. Moreover, the (Al + Mn) vs (Ti + V) ratio rises from Mag-1 to Mag-3 (Fig. 18). Such (Al + Mn) vs (Ti + V) increase has been ascribed to the pulsed injection of hydrothermal fluid at an increasing temperature similar to that observed by Zhang et al. (2020) observed in the Xinqiao Cu-Fe-Au deposit.

The subsequent increase of Sn and decrease of V contents from Mag-3 to Mag-4 reflects an increase in *f*O₂ of the system, which promoted oxyexsolution re-equilibration of Mag-3 and subsequent exsolution of oriented spinel crystals (T4 in Fig. 19d) at < 700 °C (Fig. 17a). During the retrograde stage, the former Mag-3 recrystallized to Mag-4 under conditions of decreasing temperature and assisted dynamic regime (T5 in Fig. 19d). The retrograde stage also led to the hydration of anhydrous silicates formed in the prograde stage (i.e., the transformation of forsterite to serpentine and chlorite).

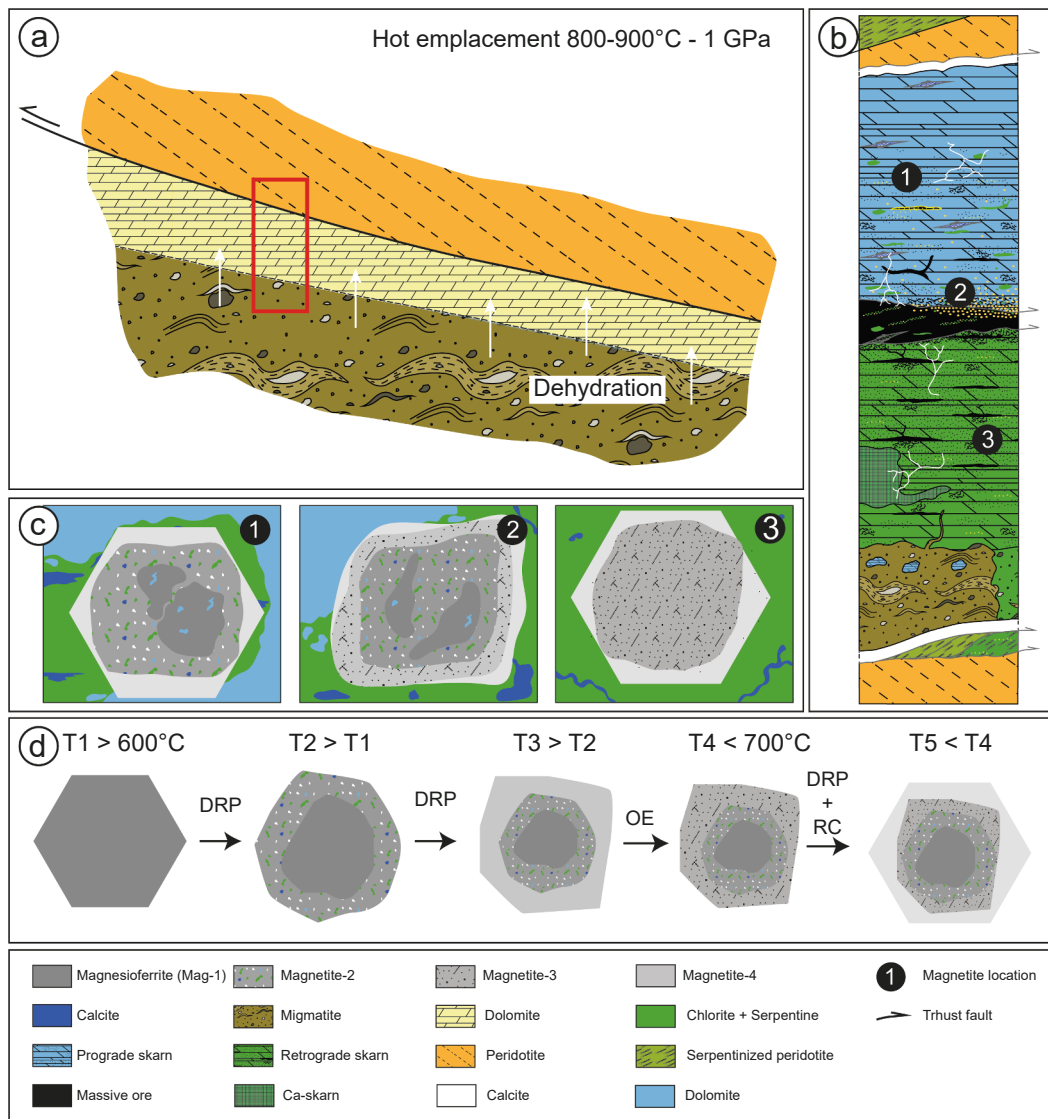


Fig. 19. Sketches showing the formation of the San Manuel deposit and associated magnetite formation and evolution (see main text for explanation).

6. Conclusions

The San Manuel skarn iron deposit is situated in a very rare geological framework involving ultramafic rocks. The hot emplacement of Ronda peridotites over crustal rocks of the Blanca Unit promoted dehydration and partial fusion of migmatite.

We ascribed the skarn and ore formation to the interaction of the migmatite-derived fluids with overlying dolomitic marbles. According to textural, major, minor, and trace element composition, and the mineralogy of the inclusions, we have defined four different generations of magnesioferrite-magnetite. Overall, there is a Fe-enrichment and Mg-depletion trend of these ore minerals during skarn evolution. Magnesioferrite (Mag-1) was the first ore mineral formed, whose composition reflects the buffer effect of the skarn host rock (i.e., dolomite). During the prograde stage of the skarn, the injection of pulsed hydrothermal fluid at increasing temperature and fluid/rock promoted disequilibrium of Mag-1 with evolving fluids, which led to coupled dissolution and reprecipitation processes, forming Mag-2 and lately Mag-3 by subsequent replacement of Mag-1 and Mag-2. Mag-3 is Al-, Ti-, V-, and Ga-rich congruent with high-temperature formation and with spinel (s.s) exsolution observed in this magnetite. We have approached a minimum temperature of the prograde stage (<700 °C), recorded by magnetite-spinel exsolution in Mag-3. During the retrograde stage, cooler and

more oxidized fluids interacted with former magnetite generations promoting disequilibrium. Microstructure, lack of inclusions, and low trace element total contents in Mag-4 rims record cooling and final dynamic fluid-assisted replacement of pre-existing magnetite of the skarn.

Declaration of Competing Interest

The authors declare that they have no known competing financial interests or personal relationships that could have appeared to influence the work reported in this paper.

Acknowledgments

This study was funded by the Spanish project RTI2018-099157-A-I00, granted by the “Ministerio de Ciencia, Innovación y Universidades”, the grant PRE2019-088262 “Ayudas para contratos predoctorales para la formación de doctores” (FPI), defrayed by the “Ministerio de Ciencia, Innovación y Universidades. The Mexican research program “CONACYT-Ciencia Básica” A1-S-14574 is also thanked for proving additional funding for standards employed in LA-ICP-MS analysis. J.M. González-Jiménez also acknowledge funding provided by the Ramón y Cajal Fellowship RYC-2015-17596. We would

like to thank X. Llovet from “Serveis Científico-Tècnics” (CCiTUB) of the Universidad de Barcelona for his invaluable assistance with the electron probe micro-analyzer, and to C. Ortega-Obregón from the “Laboratorio de Estudios Isotópicos of the Centro de Geociencias” (UNAM, Mexico) for his help with the LA-ICP-MS analyses on magnetite. Moreover, we would like to express our gratitude to I. Sánchez from the “Centro de Instrumentación Científica (CIC-UGR) for her supporting of the scanning electron microscope. The authors would like to acknowledge the use of “Servicio General de Apoyo a la Investigación-SAI, Universidad de Zaragoza”, particularly the help of C. Gallego and L. Casado Zuera from the “Advanced Microscopy Laboratory” (LMA) for their careful preparation of the EBSD maps and FIB samples, respectively.

Appendix A. Supplementary data

Supplementary data to this article can be found online at <https://doi.org/10.1016/j.oregeorev.2021.104657>.

References

- Acosta-Góngora, P., Gleeson, S.A., Samson, I.M., Ootes, L., Corriveau, L., 2014. Trace element geochemistry of magnetite and its relationship to Cu-Bi-Co-Au-Ag-U-W mineralization in the great bear magmatic zone, NWT, Canada. *Econ. Geol.* 109, 1901–1928. <https://doi.org/10.2113/econgeo.109.7.1901>.
- Acosta-Vigil, A., Rubatto, D., Bartoli, O., 2014. Age of anatexis in the crustal footwall of the Ronda peridotites, S Spain. *Lithos* 210–211, 147–167. <https://doi.org/10.1016/j.lithos.2014.08.018>.
- Andrieux, J., Fontbote, J.-M., Mattauer, M., 1971. Sur un modele explicatif de l'arc de Gibraltar. *Earth Planet. Sci. Lett.* 12 (2), 191–198. [https://doi.org/10.1016/0012-821X\(71\)90077-X](https://doi.org/10.1016/0012-821X(71)90077-X).
- Aleksandrov, S.M., Troneva, M.A., 2008. Heterovalent Isomorphism in the Magnesium-Iron Borates. *Geochem. Int.* 46 (8), 800–813. <https://doi.org/10.1134/S0016702908080053>.
- Ávila, C.F., Lagoeiro Sr, L.E., Ferreira, F.O., Graça, L.M., 2015. Crystallographic Fabrics, Grain Boundary Microstructure and Shape Preferred Orientation of Deformed Banded Iron Formations and their Significance for Deformation Interpretation. In *AGU Fall Meeting Abstracts (T41C-2917)*.
- Balanyá, J.C., García-Dueñas, V., 1987. Les directions structurales dans le Domaine d'Alborán de part et d'autre du Détroit de Gibraltar. *Comptes rendus de l'Académie des sciences. Série 2, Mécanique, Physique, Chimie, Sciences de l'univers, Sciences de la Terre*, 304(15):929–932.
- Balanyá, J.C., Crespo-Blanc, A., Azpiroz, M.D., Expósito, I., Luján, M., 2007. Structural trend line pattern and strain partitioning around the Gibraltar Arc accretionary wedge: Insights as to the mode of orogenic arc building. *Tectonics* 26 (2). <https://doi.org/10.1029/2005TC001932>.
- Bilohušćin, V., Uher, P., Koděra, P., Milovská, S., Mikuš, T., Bačík, P., 2017. Evolution of borate minerals from contact metamorphic to hydrothermal stages: Ludwigite-group minerals and szaibélyite from the Vysoká – Zlatno skarn, Slovakia. *Mineral. Petrol.* 111, 643–658. <https://doi.org/10.1007/s00710-017-0518-y>.
- Broughm, S.G., Hanchar, J.M., Tornos, F., Westhues, A., Attersley, S., 2017. Mineral chemistry of magnetite from magnetite-apatite mineralization and their host rocks: examples from Kiruna, Sweden, and El Laco, Chile. *Miner. Deposita* 52, 1223–1244. <https://doi.org/10.1007/s00126-017-0718-8>.
- Calvo, G., Tornos, F., Velasco, F., 2013. The geology of the giant Pampa del Pongo magnetite skarn (S Peru) and its relationship with IOCG systems. In: *Mineral deposit research for a high-tech World -12th SGA Biennial Meeting 2013*, pp. 1355–1358.
- Canil, D., Grondahl, C., Lacourse, T., Pisia, L.K., 2016. Trace elements in magnetite from porphyry Cu-Mo-Au deposits in British Columbia, Canada. *Ore Geol. Rev.* 72, 1116–1128. <https://doi.org/10.1016/j.oregeorev.2015.10.007>.
- Carew, M.J., 2004. Controls on Cu-Au mineralization and Fe oxide metasomatism in the Eastern fold belt, NW Queensland, Australia. *Doctoral dissertation, James Cook University*.
- Cepedal, A., Martín-Izard, A., Reguilón, R., Rodríguez-Pevida, L., Spiering, E., González-Nistal, S., 2000. Origin and evolution of the calcic and magnesian skarns hosting the El Valle-Boinás copper-gold deposit, Asturias (Spain). *J. Geochem. Explor.* 71 (2), 119–151. [https://doi.org/10.1016/S0375-6742\(00\)00149-7](https://doi.org/10.1016/S0375-6742(00)00149-7).
- Chen, F., Deng, J., Wang, Q., Huizenga, J.M., Li, G., Gu, Y., 2020. LA-ICP-MS trace element analysis of magnetite and pyrite from the Hetaoping Fe-Zn-Pb skarn deposit in Baoshan block, SW China: implications for ore-forming processes. *Ore Geol. Rev.* 117, 103309. <https://doi.org/10.1016/j.oregeorev.2020.103309>.
- Coibanu, C.L., Cook, N.J., 2004. Skarn textures and a case study: the Ocna de Fier-Gonecea orefield, Banat, Romania. *Ore Geol. Rev.* 24 (3–4), 315–370. <https://doi.org/10.1016/j.oregeorev.2003.04.002>.
- Cuevas, J., Esteban, J.J., Tubía, J.M., 2006. Tectonic implications of the granite dyke swarm in the Ronda peridotites (Betic Cordilleras, Southern Spain). *J. Geol. Society* 163 (4), 631–640. <https://doi.org/10.1144/0016-764905-038>.
- Dare, S.A.S., Barnes, S.-J., Beaudoin, G., Méric, J., Emilie, B., Potvin-Doucet, C., 2014. Trace elements in magnetite as petrogenetic indicators. *Miner. Deposita* 49 (7), 785–796. <https://doi.org/10.1007/s00126-014-0529-0>.
- Deditius, A.P., Reich, M., Simon, A.C., Suvorova, A., Knipping, J., Roberts, M.P., Rubanov, S., Dodd, A., Saunders, M., 2018. Nanogeochemistry of hydrothermal magnetite. *Contrib. Miner. Petrol.* 173, 46. <https://doi.org/10.1007/s00410-018-1474-1>.
- Dewey, J.F., Helman, M.L., Knott, S.D., Turco, E., Hutton, D.H.W., 1989. Kinematics of the western Mediterranean. *Geological Society, London, Special Publications* 45, 265–283. <https://doi.org/10.1144/GSL.SP.1989.045.01.15>.
- Dupuis, C., Beaudoin, G., 2011. Discriminant diagrams for iron oxide trace element fingerprinting of mineral deposit types. *Mineralium Deposita* 46, 319–335. <https://doi.org/10.1007/s00126-011-0334-y>.
- Durand-Delga, M., Fontboté, J.M., 1980. Le cadre structural de la Méditerranée occidentale. XXVth Intern. Geological Congress. Colloque C5: Géologie des chaînes alpines issues de la Téthys. In: *Mém. Bur. Rech. Géol. Min., Orléans*, pp. 65–85.
- Egeler, C.G., Simon, O.J., 1969. Orogenic evolution of the Betic Zone (Betic Cordilleras, Spain), with emphasis on the nappe structures. *Geol. Mijnbouw* 48 (3), 296–305.
- Einaudi, M.T., Meinert, L.D., Newberry, R.J., 1981. Skarn deposits. In: *SEG Economic Geology 75th Anniversary Volume*, pp. 317–339.
- Einaudi, M.T., Burt, D.M., 1982. Introduction, terminology, classification, and composition of skarn deposit. *Econ. Geol.* 77 (4), 745–754. <https://doi.org/10.2113/gsecongeo.77.4.745>.
- Esteban, J.J., Sánchez-Rodríguez, L., Seward, D., Cuevas, J., Tubía, J.M., 2004. The late thermal history of the Ronda area, southern Spain. *Tectonophysics* 389 (1–2), 81–92. <https://doi.org/10.1016/j.tecto.2004.07.050>.
- Esteban, J.J., Cuevas, J., Tubía, J.M., Liatí, A., Seward, D., Gebauer, D., 2007. Timing and origin of zircon-bearing chlorite schists in the Ronda peridotites (Betic Cordilleras, Southern Spain). *Lithos* 99 (1–2), 121–135. <https://doi.org/10.1016/j.lithos.2007.06.006>.
- Esteban, J.J., Cuevas, J., Vegas, N., Tubía, J.M., 2008. Deformation and kinematics in a melt-bearing shear zone from the Western Betic Cordilleras (Southern Spain). *J. Struct. Geol.* 30 (3), 380–393. <https://doi.org/10.1016/j.jsg.2007.11.010>.
- Esteban, J.J., Cuevas, J., Tubía, J.M., Sergeev, S., Larionov, A., 2010. A revised Aquitanian age for the emplacement of the Ronda peridotites (Betic Cordilleras, southern Spain). *Geol. Mag.* 148 (1), 183–187. <https://doi.org/10.1017/S0016756810000737>.
- Garrido, C.J., Bodinier, J.-L., 1999. Diversity of Mafic Rocks in the Ronda Peridotite: evidence for Pervasive Melt-Rock Reaction during Heating of Subcontinental Lithosphere by Upwelling Asthenosphere. *J. Petrol.* 40 (5), 729–754. <https://doi.org/10.1093/ptro/40.5.729>.
- Garrido, C.J., Gueydan, F., Booth-Rea, G., Precigout, J., Hidas, K., Padron-Navarta, J.A., Marchesi, C., 2011. Garnet lherzolite and garnet-spinel mylonite in the Ronda peridotite: Vestiges of Oligocene backarc mantle lithospheric extension in the western Mediterranean. *Geology* 39 (10), 927–930. <https://doi.org/10.1130/G31760.1>.
- Gervilla, F., Leblanc, M., 1990. Magmatic ores in high-temperature alpine-type lherzolite massifs (Ronda, Spain, and Beni Bousera, Morocco). *Econ. Geol.* 85 (1), 112–132. <https://doi.org/10.2113/gsecongeo.85.1.112>.
- Gervilla, F., González-Jiménez, J.M., Hidas, K., Marchesi, C., Piña, R., 2019. *Geology and Metallogeny of the Upper Mantle Rocks from the Serranía de Ronda. Mineralogical Spanish Society, Ronda*, p. 122.
- Ghosh, B., Konar, R., 2012. Textural developments in chromite deforming under eclogite-facies conditions from the Neorachean Sittampundi anorthosite complex, southern India. *Geological Journal*, 47(2-3):253–262. Special Issue: The Indian Precambrian: correlation and connections. doi:10.1002/gj.1316.
- Ghosh, B., Ray, J., Marishita, T., 2014. Grain-scale plastic deformation of chromite from podiform chromitite of the Naga-Manipur ophiolite belt, India: Implication to mantle dynamics. *Ore Geol. Rev.* 56, 199–208. <https://doi.org/10.1016/j.oregeorev.2013.09.001>.
- Ghosh, B., Misra, S., Morishita, T., 2017. Plastic deformation and post-deformation annealing in chromite: mechanisms and implications. *Am. Mineral.* 102 (1), 216–226. <https://doi.org/10.2138/am-2017-5709>.
- González-Jiménez, J.M., Villaseca, C., Griffin, W.L., Belousova, E.A., Konc, Z., Ancochea, E., O'Reilly, S.Y., Pearson, N.J., Garrido, C.J., Gervilla, F., 2013a. The architecture of the European-Mediterranean lithosphere: a synthesis of the Re-Os evidence. *Geology* 41 (5), 547–550. <https://doi.org/10.1130/G34003.1>.
- González-Jiménez, J.M., Marchesi, C., Griffin, W.L., Gutiérrez-Narbona, R., Lorand, J.-P., O'Reilly, S.Y., Garrido, C.J., Gervilla, F., Pearson, N.J., Hidas, K., 2013b. Transfer of Os isotopic signatures from peridotite to chromitite in the subcontinental mantle: insights from in situ analysis of platinum-group and base-metal minerals (Ojén peridotite massif, southern Spain). *Lithos* 164–167, 74–85. <https://doi.org/10.1016/j.lithos.2012.07.009>.
- González-Jiménez, J.M., Marchesi, C., Griffin, W.L., Gervilla, F., Belousova, E.A., Garrido, C.J., Romero, R., Talavera, C., Leisen, M., O'Reilly, S.Y., Barra, F., Martín, L., 2017. Zircon recycling and crystallization during formation of chromite- and Ni-arsenide ores in the subcontinental lithospheric mantle (Serranía de Ronda, Spain). *Ore Geol. Rev.* 90, 193–209. <https://doi.org/10.1016/j.oregeorev.2017.02.012>.
- González-Jiménez, J.M., Colás, V., Gervilla, F., Kerestedjian, T.N., Sergeeva, I., Casado-González, A., Fanlo, I., 2018. Metamorphic evolution of sulphide-rich chromitites from the Chernichevo ultramafic massif, SE Bulgaria. *Ore Geol. Rev.* 101, 330–348. <https://doi.org/10.1016/j.oregeorev.2018.07.024>.
- Graf, D.L., 1961. Crystallographic tables for the rhombohedral carbonates. *Am. Mineral.* 46 (11–12), 1283–1316.
- Guo, X., Jia, Q., Lü, X., Li, J., Kong, H., Yao, X., 2020. The Permian Sn metallogenic event and its geodynamic setting in East Kunlun, NW China: Evidence from zircon and cassiterite geochronology, geochemistry, and Sr-Nd-Hf isotopes of the Xiaowolong

- skarn Sn deposit. *Ore Geol. Rev.* 118, 103370 <https://doi.org/10.1016/j.oregeorev.2020.103370>.
- Halfpenny, A., Prior, D.J., Wheeler, J., 2006. Analysis of dynamic recrystallization and nucleation in a quartzite mylonite. *Tectonophysics* 427 (1–4), 3–14. <https://doi.org/10.1016/j.tecto.2006.05.016>.
- Hidas, K., Booth-Rea, G., Garrido, C.J., Martínez-Martínez, J.M., Padrón-Navarta, J.A., Konc, Z., Giaconia, F., Frets, E., Marchesi, C., 2013. Backarc basin inversion and subcontinental mantle emplacement in the crust: kilometer-scale folding and shearing at the base of the proto-Alborán lithospheric mantle (Betic Cordillera, southern Spain). *J. Geol. Society* 170 (1), 47–55. <https://doi.org/10.1144/jgs2011-151>.
- Hidas, K., Varas-Reus, M.I., Garrido, C.J., Marchesi, C., Acosta-Vigil, A., Padrón-Navarta, J.A., Targuisti, K., Konc, Z., 2015. Hyperextension of continental to oceanic-like lithosphere: The record of late gabbros in the shallow subcontinental lithospheric mantle of the westernmost Mediterranean. *Tectonophysics* 650, 65–79. <https://doi.org/10.1016/j.tecto.2015.03.011>.
- Hey, M.H., 1954. A new review of the chlorites. *Mineral. Mag. J. Mineral. Society* 30 (224), 277–292.
- Hu, H., Li, J.-W., Lentz, D., Ren, Z., Zhao, X.-F., Deng, X.-D., Hall, D., 2014. Dissolution–reprecipitation process of magnetite from the Chengchao iron deposit: Insights into ore genesis and implication for in-situ chemical analysis of magnetite. *Ore Geol. Rev.* 57, 393–405. <https://doi.org/10.1016/j.oregeorev.2013.07.008>.
- Hu, H., Lentz, D., Li, J.-W., et al., 2015. Re-equilibration processes in magnetite from iron skarn deposits. *Econ. Geol.* 110 (1), 1–8. <https://doi.org/10.2113/econgeo.110.1.1>.
- Hu, X., Chen, H., Zhao, L., Han, J., Xia, X., 2017. Magnetite geochemistry of the Longqiao and Tieshan Fe–(Cu) deposits in the Middle-Lower Yangtze River Belt: implications for deposit type and ore genesis. *Ore Geol. Rev.* 89, 822–835. <https://doi.org/10.1016/j.oregeorev.2017.07.019>.
- Hu, H., Li, J.-W., Harlov, D., Lentz, D., McFarlane, C., Yang, Y.H., 2020. A genetic link between iron oxide-apatite and iron skarn mineralization in the Jinniu volcanic basin, Daye district, eastern China. *GSA Bulletin* 132 (5–6), 899–917. <https://doi.org/10.1130/B35180.1>.
- Huang, X.-W., Gao, J.-F., Qi, L., et al., 2016. In-situ LA-ICP-MS trace elements analysis of magnetite: The Fenghuangshan Cu–Fe–Au deposit, Tongling, Eastern China. *Ore Geol. Rev.* 72 (1), 746–759. <https://doi.org/10.1016/j.oregeorev.2015.09.012>.
- Huang, X.W., Boutroy, E., Makvandi, S., Beaudoin, G., Corriveau, L., De Toni, A.F., 2019. Trace element composition of iron oxides from IOCG and IOA deposits: relationship to hydrothermal alteration and ore deposit subtypes. *Miner. Deposita* 54, 525–552. <https://doi.org/10.1007/s00126-018-0825-1>.
- Jansson, N.F., Allen, R.L., 2015. Multistage ore formation at the Ryllshyttan marble and skarn-hosted Zn–Pb–Ag–(Cu)+magnetite deposit, Bergslagen, Sweden. *Ore Geol. Rev.* 69, 217–242. <https://doi.org/10.1016/j.oregeorev.2015.02.018>.
- Kuşçu, İ., (2019) Skarns and Skarn Deposits of Turkey. In: Pirajno, F., Ünlü, T., Dönmez, C., Şahin, M. (eds) Mineral Resources of Turkey. Modern Approaches in Solid Earth Sciences, vol 16. Springer, Cham. doi:10.1007/978-3-030-02950-0-7.
- Leake, B.E., Woolley, A.R., Birch, W.D., Burke, E.A.J., Ferraris, G., Grice, J.D., et al., 2004. Nomenclature of amphiboles: additions and revisions to the International Mineralogical Association's amphibole nomenclature. *Am. Mineral.* 68 (1), 209–215. <https://doi.org/10.1180/0026461046810182>.
- Lehmann, J., Roux, J., 1986. Experimental and theoretical study of (Fe²⁺, Mg) (Al, Fe³⁺)₂O₄ spinels: Activity-composition relationship, miscibility gaps, vacancy contents. *Geochim. Cosmochim.* 50, 1765–1783.
- Lindsley, D.H., 1991. Oxide Minerals: Petrologic and Magnetic Significance. De Gruyter.
- Logan, M.A.V., 2000. Mineralogy and geochemistry of the Gualilán skarn deposit in the Precordillera of western Argentina. *Ore Geol. Rev.* 17 (1–2), 113–138. [https://doi.org/10.1016/S0169-1368\(00\)00009-3](https://doi.org/10.1016/S0169-1368(00)00009-3).
- Mao, J., Zhou, Y., Liu, H., et al., 2017. Metallogenic setting and ore genetic model for the Beiya porphyry-skarn polymetallic Au orefield, western Yunnan, China. *Ore Geol. Rev.* 86, 21–34. <https://doi.org/10.1016/j.oregeorev.2017.02.003>.
- Marchesi, C., Griffin, W.L., Garrido, C.J., et al., 2010. Persistence of mantle lithospheric Re–Os signature during asthenospherization of the subcontinental lithospheric mantle: insights from in situ isotopic analysis of sulfides from the Ronda peridotite (Southern Spain). *Contrib. Miner. Petrol.* 159, 315–330. <https://doi.org/10.1007/s00410-009-0429-y>.
- Marchesi, C., Garrido, C.J., Bosch, D., et al., 2012. A Late Oligocene suprasubduction setting in the westernmost Mediterranean revealed by intrusive pyroxenite dikes in the Ronda peridotite (southern Spain). *J. Geol.* 120 (2), 237–247. <https://doi.org/10.1086/663875>.
- Marincea, S., Dumitras, D.-G., 2019. Contrasting types of boron-bearing deposits in magnesian skarns from Romania. *Ore Geol. Rev.* 112, 102952 <https://doi.org/10.1016/j.oregeorev.2019.102952>.
- Mazzoli, S., Martín-Algarra, A., Reddy, S.M., et al., 2013. The evolution of the footwall to the Ronda subcontinental mantle peridotites: insights from the Nieves Unit (western Betic Cordillera). *J. Geol. Society* 170 (3), 385–402. <https://doi.org/10.1144/jgs2012-105>.
- McSwiggen, P.L., 1993a. Alternative solution model for the ternary carbonate system CaCO₃–MgCO₃–FeCO₃. Part 1. A ternary Bragg–Williams ordering model. *Phys. Chem. Miner.* 20, 33–41. <https://doi.org/10.1007/BF00202248>.
- McSwiggen, P.L., 1993b. Alternative solution model for the ternary carbonate system CaCO₃–MgCO₃–FeCO₃. Part 2. Calibration of a combined ordering model and mixing model. *Phys. Chem. Miner.* 20, 42–55. <https://doi.org/10.1007/BF00202249>.
- Mei, W., Lü, X., Wang, X., et al., 2017. Geochemistry of magnetite from the Huanggang skarn iron-tin polymetallic deposit in the southern Great Xing'an Range, NE China. *Geol. J.* (3), 1200–1241. <https://doi.org/10.1002/gj.2951>.
- Meinert, L.D., 1992. Skarns and Skarn Deposits. *Geosci. Can.* 19, 145–162.
- Meinert, L.D., Dipple, G.M., Nicolescu, S., 2005. World skarn deposits. *Econ. Geol.* 100, 299–336. <https://doi.org/10.5382/AV100.11>.
- Mirzaei, R., Ahmadi, A., Mirnejad, H., et al., 2018. Two-tiered magmatic-hydrothermal and skarn origin of magnetite from Gol-Gohar iron ore deposit of SE Iran: in-situ LA-ICP-MS analyses. *Ore Geol. Rev.* 102, 639–653. <https://doi.org/10.1016/j.oregeorev.2018.09.025>.
- Morishita, T., Arai, S., Gervilla, F., 2001. High-pressure aluminous mafic rocks from the Ronda peridotite massif, southern Spain: significance of sapphirine- and corundum-bearing mineral assemblages. *Lithos* 57 (2–3), 143–161. [https://doi.org/10.1016/S0024-4937\(01\)00036-6](https://doi.org/10.1016/S0024-4937(01)00036-6).
- Nadol, P., Mauk, J.F., Hayes, T.S., Koenig, A.E., Box, S.E., 2012. Geochemistry of Magnetite from Hydrothermal Ore Deposits and Host Rocks of the Mesoproterozoic Belt Supergroup, United States. *Econ. Geol.* 107 (6), 1275–1292. <https://doi.org/10.2113/econgeo.107.6.1275>.
- Nadol, P., Angerer, T., Mauk, J.L., French, D., Walshe, J., 2014. The chemistry of hydrothermal magnetite: A review. *Ore Geol. Rev.* 61, 1–32. <https://doi.org/10.1016/j.oregeorev.2013.12.013>.
- Nadol, P., Mauk, J.L., Leveille, R.A., Koenig, A.E., 2015. Geochemistry of magnetite from porphyry Cu and skarn deposits in the southwestern United States. *Miner. Deposita* 50, 493–515. <https://doi.org/10.1007/s00126-014-0539-y>.
- Navarro-Vilá, F., Tubía, J.M., 1983. Essai d'une nouvelle différentiation des Nappes Alpujarrides dans le secteur occidental des Cordillères Bétiques (Andalousie, Espagne). *CR Académie des Sciences, Paris*, 296 (série II), pp. 111–114.
- Nord, A.G., Annersten, H., Filippidis, A., 1982. The cation distribution in synthetic Mg–Fe–Ni olivines. *Am. Mineral.* 67, 1206–1211.
- Obata, M., 1980. The Ronda peridotite-garnet-lherzolite, spinel-lherzolite, and plagioclase-lherzolite facies and the PT trajectories of a high-temperature mantle intrusion. *J. Petrol.* 21 (3), 533–572.
- Pereira, M.D., Shaw, D.M., Acosta, A., 2003. Mobile trace elements and fluid-dominated processes in the Ronda peridotite, southern Spain. *Can. Mineral.* 41 (3), 617–625. <https://doi.org/10.2113/gscanmin.41.3.617>.
- Platt, J.P., Behr, W.M., Johanesen, K., Williams, J.R., 2013. The Betic-Rif arc and its orogenic hinterland: a review. *Annu. Rev. Earth Planet. Sci.* 41, 313–357.
- Pons, J., Franchini, M., Meinert, L., López-Escobar, L., Maydagán, L., 2010. Geology, petrography and geochemistry of igneous rocks related to mineralized skarns in the NW Neuquén basin, Argentina: implications for Cordilleran skarn exploration. *Ore Geol. Rev.* 38 (1–2), 37–58. <https://doi.org/10.1016/j.oregeorev.2010.05.006>.
- Popović, J., Tkáčec, E., Grzeta, B., et al., 2009. Inverse spinel structure of Co-doped gahnite. *Am. Mineral.* 94, 771–776. <https://doi.org/10.2138/am.2009.3173>.
- Precigout, J., Gueydan, F., Gapais, D., Garrido, C.J., Essaifi, A., 2007. Strain localisation in the subcontinental mantle — a ductile alternative to the brittle mantle. *Tectonophysics* 445 (3–4), 318–336. <https://doi.org/10.1016/j.tecto.2007.09.002>.
- Rapp, J.F., Klemme, S., Butler, I.B., Harley, S.L., 2010. Extremely high solubility of rutile in chloride and fluoride-bearing metamorphic fluids: An experimental investigation. *Geology* 38, 323–326. <https://doi.org/10.1130/G30753.1>.
- Reisberg, L., Lorand, J.P., 1995. Longevity of sub-continental mantle lithosphere from osmium isotope systematics in orogenic peridotite massifs. *Nature* 376, 159–162. <https://doi.org/10.1038/376159a0>.
- Righter, K., Leeman, W.P., Hervig, R.L., 2006. Partitioning of Ni, Co and V between spinel-structured oxides and silicate melts: importance of spinel composition. *Chem. Geol.* 227 (1–2), 1–25. <https://doi.org/10.1016/j.chemgeo.2005.05.011>.
- Rosière, C.A., Siemes, H., Quade, H., et al., 2001. Microstructures, textures and deformation mechanisms in hematite. *J. Struct. Geol.* 23 (9), 1429–1440. [https://doi.org/10.1016/S0191-8141\(01\)00009-8](https://doi.org/10.1016/S0191-8141(01)00009-8).
- Sack, R.O., Ghiorso, M.S., 1991a. Chromian spinel as petrogenetic indicators: thermodynamics and petrological applications. *Am. Mineral.* 76, 827–847.
- Sack, R.O., Ghiorso, M.S., 1991b. An internally consistent model for the thermodynamic properties of Fe–Mg–titanomagnetite–aluminite spinels. *Contrib. Miner. Petrol.* 106, 474–505.
- Sanchez-Rodríguez, L., 1998. Pre-Alpine and Alpine evolution of the Ronda ultramafic complex and its country-rocks (Betic chain, southern Spain): U–Pb SHRIMP zircon and fission-track dating. (Doctoral dissertation, ETH Zurich). doi:10.3929/ethz-a-002057996.
- Sarjoughian, F., Habibi, I., Lentz, D., et al., 2020. Magnetite compositions from the Baba Ali iron deposit in the Sanandaj–Sirjan zone, western Iran: Implications for ore genesis. *Ore Geol. Rev.* 126, 103728 <https://doi.org/10.1016/j.oregeorev.2020.103728>.
- Satsukawa, T., Piazzol, S., González-Jiménez, J.M., et al., 2015. Fluid-present deformation aids chemical modification of chromite: Insights from chromites from Golyamo Kamenyane, SE Bulgaria. *Lithos* 228–229, 78–89. <https://doi.org/10.1016/j.lithos.2015.04.020>.
- Sun, X., Lin, H., Fu, Y., et al., 2017. Trace element geochemistry of magnetite from the giant Beiya gold-polymetallic deposit in Yunnan Province, Southwest China and its implications for the ore forming processes. *Ore Geol. Rev.* 91, 477–490. <https://doi.org/10.1016/j.oregeorev.2017.09.007>.
- Toplis, M.J., Corgne, A., 2002. An experimental study of element partitioning between magnetite, clinopyroxene and iron-bearing silicate liquids with particular emphasis on vanadium. *Contrib. Miner. Petrol.* 144, 22–37. <https://doi.org/10.1007/s00410-002-0382-5>.
- Torres-Roldán, R.L., 1983. Fractionated melting of metapelite and further crystal-melt equilibria—the example of the Blanca Unit migmatite complex, north of Estepona (southern Spain). *Tectonophysics* 96 (1–2), 95–123. [https://doi.org/10.1016/0040-1951\(83\)90246-9](https://doi.org/10.1016/0040-1951(83)90246-9).
- Tubía, J.M., Cuevas, J., 1986. High-temperature emplacement of the Los Reales peridotite nappe (Betic Cordillera, Spain). *J. Struct. Geol.* 8 (3–4), 473–482. [https://doi.org/10.1016/0191-8141\(86\)90064-7](https://doi.org/10.1016/0191-8141(86)90064-7).

- Tubía, J.M., Cuevas, J.M., Ibarra, J.I.G., 1997. Sequential development of the metamorphic aureole beneath the Ronda peridotites and its bearing on the tectonic evolution of the Betic Cordillera. *Tectonophysics* 279 (1–4), 227–252. [https://doi.org/10.1016/S0040-1951\(97\)00124-8](https://doi.org/10.1016/S0040-1951(97)00124-8).
- Tubía, J.M., Cuevas, J., Esteban, J.J., 2013. Localization of deformation and kinematic shift during the hot emplacement of the Ronda peridotites (Betic Cordilleras, southern Spain). *J. Struct. Geol.* 50, 148–160. <https://doi.org/10.1016/j.jsg.2012.06.010>.
- Van der Wal, D., Vissers, R.L.M., 1993. Uplift and emplacement of upper mantle rocks in the western Mediterranean. *Geology* 21 (12), 1119–1122. [https://doi.org/10.1130/0091-7613\(1993\)021<1119:UAEOUM>2.3.CO;2](https://doi.org/10.1130/0091-7613(1993)021<1119:UAEOUM>2.3.CO;2).
- Van der Wal, D., Vissers, R.L.M., 1996. Structural Petrology of the Ronda Peridotite, SW Spain: Deformation History. *J. Petrol.* 37 (1), 23–43. <https://doi.org/10.1093/ptrology/37.1.23>.
- Velasco, F., Tornos, F., Hanchar, J.M., 2016. Immiscible iron- and silica-rich melts and magnetite geochemistry at the El Laco volcano (northern Chile): Evidence for a magmatic origin for the magnetite deposits. *Ore Geol. Rev.* 79, 346–366. <https://doi.org/10.1016/j.oregeorev.2016.06.007>.
- Vissers, R.L.M., Platt, J.P., Van der Wal, D., 1995. Late orogenic extension of the Betic Cordillera and the Alborán Domain: A lithospheric view. *Tectonics* 14 (4), 786–803. <https://doi.org/10.1029/95TC00086>.
- Wang, C., Shao, Y., Zhang, X., et al., 2018. Trace Element Geochemistry of Magnetite: implications for Ore Genesis of the Huanggangliang Sn-Fe Deposit, Inner Mongolia, Northeastern China. *Minerals* 8 (5), 195. <https://doi.org/10.3390/min8050195>.
- Wechsler, B.A., Lindsley, D.H., Prewitt, C.T., 1984. Crystal structure and cation distribution in titanomagnetites (Fe_{3-x}Ti_xO₄). *Am. Mineral.* 69 (7–8), 754–770.
- Whitney, D.L., Evans, B.W., 2010. Abbreviations for names of rock-forming minerals. *Am. Mineral.* 95 (1), 185–187. <https://doi.org/10.2138/am.2010.3371>.
- Xie, Q., Mao, J., Zhu, Q., Yao, L., Li, Y., Li, W., Zhao, H., 2015. Geochemical constraints on Cu–Fe and Fe skarn deposits in the Edong district, Middle-Lower Yangtze River metallogenic belt, China. *Ore Geol. Rev.* 64, 425–444. <https://doi.org/10.1016/j.oregeorev.2014.08.005>.
- Xie, G.Q., Mao, J.W., Richards, J.P., Han, Y.X., Fu, B., 2019. Distal Au deposits associated with Cu–Au skarn mineralization in the Fengshan area, eastern China. *Econ. Geol.* 114, 127–142. <https://doi.org/10.5382/econgeo.2019.4623>.
- Xie, Q.H., Zhang, Z.C., Jin, Z.L., Santosh, M., Liu, H., Wang, K.Y., Zhao, P.L., He, H.H., 2021. The high-grade Fe skarn deposit of Jinling, North China Craton: insights into hydrothermal iron mineralization. *Ore Geol. Rev.* 138, 104395. <https://doi.org/10.1016/j.oregeorev.2021.104395>.
- Yu, M., 2019. Metallogenic Mechanism of the Galinge Polymetallic Iron Skarn Deposit, Qiman Tagh Mountains, Qinghai Province. In: *Metallogenic Mechanism of the Galinge Polymetallic Iron Skarn Deposit, Qiman Tagh Mountains, Qinghai Province*. Springer Theses (Recognizing Outstanding Ph.D. Research). Springer, Singapore. doi:10.1007/978-981-10-7907-8_10.
- Zhang, Z., Du, Y., Zhang, J., 2013. Alteration, mineralization, and genesis of the zoned Tongshan skarn-type copper deposit, Anhui, China. *Ore Geol. Rev.* 53 (3), 489–503.
- Zhang, Z.C., Hou, T., Santosh, M., Li, H.M., Li, J.W., Zhang, Z.H., Song, X.Y., Wang, M., 2014. Spatio-temporal distribution and tectonic settings of the major iron deposits in China, An overview. *Ore Geol. Rev.* 57, 247–263. <https://doi.org/10.1016/j.oregeorev.2013.08.021>.
- Zhang, Y., Hollings, P., Shao, Y., Li, D., Chen, H., Li, H., 2020. Magnetite texture and trace-element geochemistry fingerprint of pulsed mineralization in the Xinqiao Cu–Fe–Au deposit, Eastern China. *Am. Mineral.: J. Earth Planet. Mater.* 105 (11), 1712–1723. <https://doi.org/10.2138/am-2020-7414>.
- Zhang, Z.C., Li, H.M., Li, J.W., Song, X.Y., Hu, H., Li, L.X., Chai, F.M., Hou, T., Xu, D.R., 2021. Geological settings and metallogenesis of high-grade iron deposits in China. *Science China* 64, 691–715. <https://doi.org/10.1007/s11430-020-9735-5>.
- Zhao, W.W., Zhou, M.-F., Li, Y.H.M., Zhao, Z., Gao, J.-F., 2017. Genetic types, mineralization styles, and geodynamic settings of Mesozoic tungsten deposits in South China. *J. Asian Earth Sci.* 137, 109–140. <https://doi.org/10.1016/j.jseaes.2016.12.047>.
- Zharikov, V.A., 1970. Skarns. *International Geological Review* 12, 544–559, 6, 619–674, 7, 760–775.
- Zharikov, V.A., Pertsev, N.N., Rusinov, V.L., Callegari, E., Fettes, D.J., 2007. *Metasomatism and metasomatic rocks, Recommendations by the IUGS subcommission on the systematics of metamorphic rocks*, 9.